5

Infrared Radiation Photodetectors

Ashraf S. A. Nasr[1,2]
[1]*Radiation Engineering Dept., NCRRT, Atomic Energy Authority, Cairo,*
[2]*College of Computer Science, Qassim University, Buryadah,*
[1]*Egypt*
[2]*Kingdom of Saudi Arabia*

1. Introduction

Nanotechnology is regarded world-wide as one of the key technologies of the *21st* century. Nanotechnological products and processes hold an enormous economic potential for the markets of the future. The production of ever smaller, faster and more efficient products with acceptable price-to-performance ratio has become for many industrial branches an increasingly important success factor in the international competition. The technological competence in nanotechnology will be a compelling condition to compete successfully with better procedures and products on high technology markets in the future. Due to its interdisciplinary cross-section character, nanotechnology will affect broad application fields within the ranges of chemistry/materials, medicine/life sciences, electronics/ information technology, environmental and energy engineering, automotive manufacturing as well as optics/analytics and precision engineering in various ways (Aboshosha et al., 2009a; Aboshosha et al., 2009b; Abou El-Fadl et al., 1998; Eladle et al., 2009; Nasr, El_mashade, 2006; El_mashade et al., 2003; El_mashade et al., 2005; Future Technologies Division, 2003; Nasr, 2011; Nasr, 2011b; Nasr, 2009; Nasr et al., 2009; Nasr, 2008; Nasr,2006; Nasr & Ashry; 2000).

One of the considered devices which had witness the development is IR photodetectors. A photodetector is an electronic device that converts incident photons into electric current. Photodetectors have a wide range of scientific and consumer applications and have played a central role in the development of modern physics during the last century (Ryzhii, 2003).

Photodetectors are classified according to their optical range which can be covered. As we can see in Fig. 1, the electromagnetic spectrum in the optical start regarding wavelength from UV, visible, and IR ranges (Buckner, 2008). But it is evident to notice that the visible range is small. So, it will be impeded some time into UV or/ and IR detectors. The main two types then are UV and IR photodetectors. The two types of semiconductor-based photodetectors will be reviewed here. The main problem is appearing at long wavelength optical range as the required energy gap should be small. As a result of the previous note, the required band gap materials which cover this region have very high cost. And, it is faces a complexity into the fabrication processes. The trend of the world was directed to nanotechnology (quantum) photodetectors to overcome the previous drawbacks. As a result, the review is directed to the quantum IR photodetectors (QIRPs) like quantum well, dot, and wire infrared photodetectors (QWIPs, QDIPs and QRIPs) respectively. They open the way to overcome main problems in commercial utilized IR photodetectors such as

HgCdTe photodetectors. Although QIRPs solve many problems but they suffer from other disadvantages that are illustrated into the following subsections.

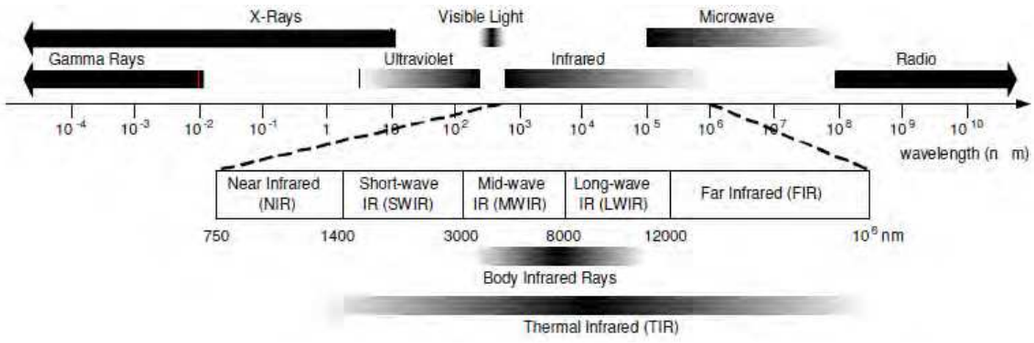

Fig. 1. The electromagnetic spectrum and the IR region (Buckner, 2008).

2. History of nanoscience & nanotechnology

Ever since man started taking control of the environment and shaping things to meet human needs, he has endeavored to understand matter at its fundamental level (Nai-Chang, 2008). Since the dawn of 21stcentury, it has become possible to study, design, and synthesize structures with the precision of one billionth of a meter (nanometer). Nanoscience is the study of the fundamentals principle of matter at scale of ~1-100 nm, while nanotechnology is the applications of such knowledge to making materials and devices (National Nanotechnology Initiative Workshop, 2004).

In December 1959, Feynman gave a visionary speech at Caltech, entitled "There is Plenty of Room at the Bottom" (URL http://www.its.caltech.edu/~feynman/). This speech was unique and held a defining place in the field now known as nanoscience and nanotechnology. In approximately 7,000 words, Feynman projected a vision that is only beginning to be realized today: "*What I want to talk about is the problem of manipulating and controlling things at a small scale… What I have demonstrated is that there is room – that you can decrease the size of things in a practical way. I now want to show that there is plenty of room. I will not now discuss how we are going to do it, but only what is possible in principle – in other words, what is possible according to the laws of physics.*" Since the historical speech, there has been significant progress to date in this highly interdisciplinary research area now known as nanoscience and nanotechnology. Not only that Feynman's vision of manipulating and controlling things down to nano- and even atomic scale becomes realizable, but novel nano-scale devices and characterization tools have also revolutionized means to exploring new science and developing new technology in a wide variety of research fields. While steady progress towards miniaturizing physical structures and tools has been made since Feynman's visionary speech and collective efforts have reached a new pinnacle since former President Bill Clinton gave his special scientific and technological strategic speech at Caltech in 1999, the strong interdisciplinary nature of nanoscience and nanotechnology is still being constant redefined and is full of both excitement and uncertainties.

3. Photodetectors fabrication techniques

It is evident to explain the advanced fabrications processes before exposing to types of photodetectors as it will help us to recognize the development which has happened in the last decades.

3.1 General nano-fabrication classifications

In general, the nano-fabrication techniques may be categorized into two types: the "top-down" and "bottom-up" approaches. The top-down approach is primarily based on lithographic techniques, including the traditional optical and electron-beam lithography for processing inorganic materials such as semiconductors, metals and dielectric/ferroelectric materials. The bottom-up approach includes the nano-imprint lithography for cross-bar architecture (Nai-Chang, 2008; Jung et al., 2006), chemical lithography for self-assembled circuits, stamping techniques for processing organic materials, multilayer soft lithography (MSL) for handling fluidic samples, and scanning probe-based lithography (SPL) that offers novel means to manipulate matter down to molecular and even atomic scale. The nano-imprint lithography may involve the use of e-beam lithography in the processing of the mold for pattern transfer (Jung et al., 2006). Recently nano-scale pitched layers of GaAs/GaAlAs superlattices have been employed for the mold, which enable efficient fabrication of high-density metallic and semiconducting nanowires and crossbar arrays (Jung et al., 2006). Here, this chapter is concentrated into the top down approach for fabrication a semiconductor-based photodetectors.

3.2 Epitaxy method

The word epitaxy refers to the ordered growth of a crystalline material on top of a crystalline substrate, such that the crystal lattice of the new layer is in registration with that of the substrate, see Fig. 2 (Muhammad et al., 2007). Epitaxial semiconductor layers are used in most semiconductor device fabrication processes because of the ability to accurately control crystal composition and doping and to form atomically abrupt hetero-interfaces. The techniques for epitaxial growth have typically been divided into processes that deliver the molecules for crystal growth in the liquid phase (LPE), deliver in the gas phase, or processes that deliver the molecules in a vacuum chamber in molecular beams. Depending on the technique, the atoms for crystal growth arrive as elemental species or within precursor molecules that thermally or chemically decompose on the surface to leave the desired species for epitaxy (Donkor, 2004).

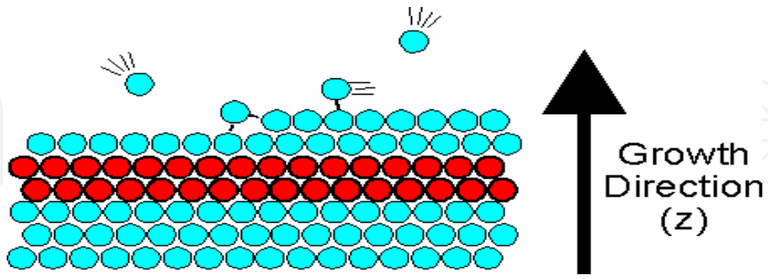

Fig. 2. The ordered, epitaxial growth of a crystalline material on a substrate (Donkor, 2004).

Epitaxial growth was divided into three major techniques. Frank and van der Merwe (Donkor, 2004) used elasticity theory to derive the concept of a critical misfit below which monolayer-by-monolayer growth appears. Volmer and Weber (Donkor, 2004), applying nucleation theory, assumed that crystalline films grew from 3D nuclei on the substrate and that their relative number and growth rate were determined by interfacial and surface free energies. The third model by Stranski and Krastanov (Brune, 2001) was based on atomistic

calculations and assumed that initially a few pseudomorphic 2D layers are formed, on top of which 3D crystal with their natural lattice constant will grow. Each of the three scenarios is observed, they rise to the following labeling of the three growth modes of epitaxy:

i. Frank-van der Merwe (FW) growth mode (2D morphology, layer-by-layer or step- flow growth).
ii. Volmer-Weber (VW) growth mode (3D morphology, island growth).
iii. Stranski-Krastanov (SK) growth mode (initially 2D, after critical thickness, 3D morphology, layer-plus-island growth).

Various technique are used for growing epitaxial layer using these three modes, but the new crystal growth techniques been used are Molecular Beam Epitaxy, MBE (Liang et al., 2006; Liu, 1993; Krost et al., 1999; Coleman, 1997) and Metal Organic Chemical Vapor Deposition, MOCVD. MOCVD is also referred to, and used interchangeably with, MOVPE/OMVPE (Metallorganic /Organometallic Vapor Phase Epitaxy). MOCVD is a broader term that is applicable to the deposition of crystal, polycrystalline and amorphous materials. Both MBE and MOCVD have produce a wide range of very high-purity semiconductor materials with excellent optical and electrical properties.

3.3 Molecular Beam Epitaxy (MBE)

MBE is an Ultra-High-Vacuum (UHV)-based technique for producing high quality epitaxial structures with monolayer (ML) control. Since its introduction in the 1970s as a tool for growing high-purity semiconductor films, MBE has evolved into one of the most widely used techniques for producing epitaxial layers of metals, insulators and superconductors as well, both at the research and the industrial production level (Muhammad et al., 2007). The principle underlying MBE growth is relatively simple: it consists essentially of atoms or clusters of atoms, which are produced by heating up a solid source. They then migrate in an UHV environment and impinge on a hot substrate surface, where they can diffuse and eventually incorporate into the growing film as in Fig. 3.

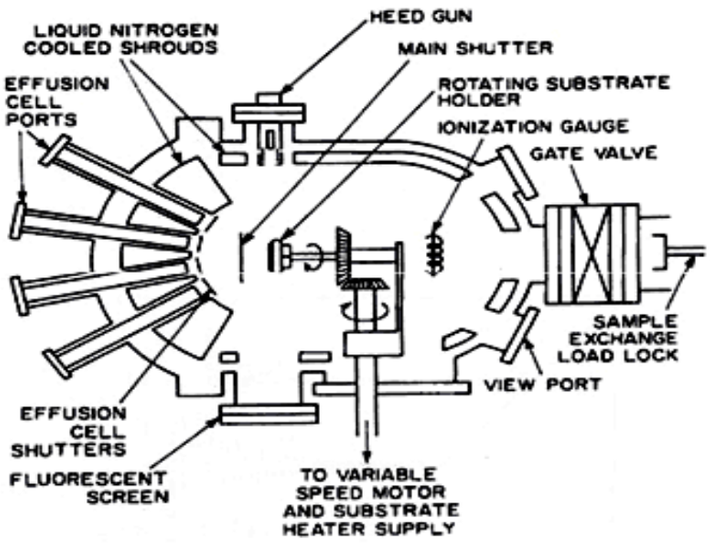

Fig. 3. Cut-away view of a modern MBE system viewed from the top (Chang & Kai, 1994).

The growth of uniform epitaxial films from multiple effusion cells requires special effusion cell geometry and continuous rotation of the substrate around an axis normal to the substrate surface. The substrate holder can feature rotation speeds up to 125 rpm. The control unit remotely orients the sample holder into any of hour positions: growth, transfer, electron beam (EB), auxiliary. The controller also allows remote continual adjustment of rotation speed. The modern commercial MBE growth chamber (Fig. 4) is often equipped with a rotary substrate manipulator capable of turning the substrate azimuthally during growth. With this feature the substrate can be heated more uniformly, resulting in epilayers of very good thickness and doping uniformity (Chang & Kai, 1994; Lee, 2005).

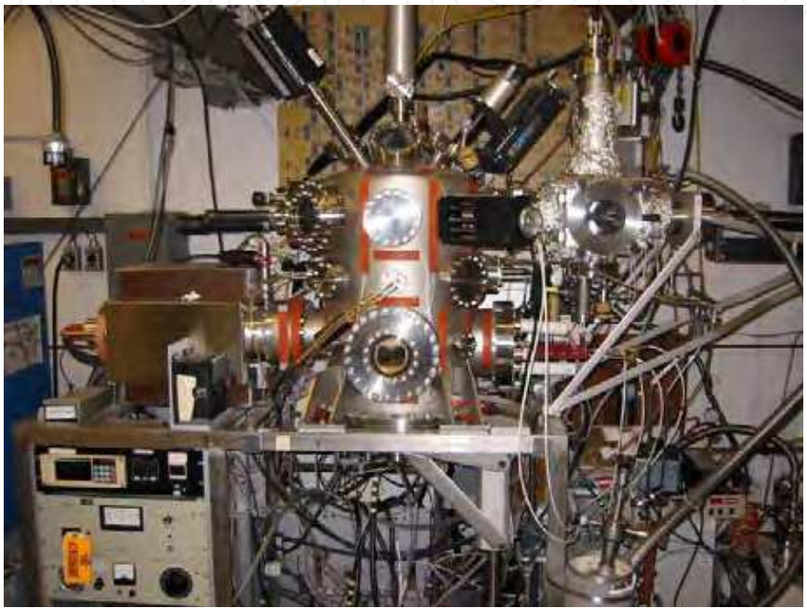

Fig. 4. MBE System at MIT, Cambridge (Lee, 2005).

3.4 Metal Organic Chemical Vapor Deposition (MOCVD)

The growth process in MOCVD is similar to MBE, but the atoms are carried in gaseous form to the substrate as shown in Fig. 5. For example, to grow epitaxial GaAs, the gasses can be trim ethyl gallium and arsine. These precursor molecules thermally decompose on the hot substrate, the resulting organic molecules evaporate, leaving the Ga and As atoms for incorporation into the crystal. Typical growth temperatures are 600^{o}C, and the growth rates are on-the-order-of 1 molecular layer of GaAs per second. This growth rate allows the precursor gasses to be switched quickly enough to give very abrupt material interfaces. The growth process given by $(CH_3)_3Ga + AsH_3 \rightarrow GaAs + 3CH_4$

The most important organometallic compounds that have been studied are trim ethyl gallium (TMGa), trim ethyl aluminum (TMAl) and trim ethyl indium (TMIn). These sources should be easily synthesized and easily purified related to practicalities of using several different sources together (Coleman, 1997). In general, the organometallic constituents are transported to a heated substrate by passing a carrier gas, usually hydrogen or nitrogen or a mixture of the two, over or through the compound contained in a constant-temperature bubbler vessel. Most MOCVD growth of III-V compound semiconductors and alloys

involves the use of hydrides, such as arsine or phosphine, for the column V species because they are already gaseous and supplied from simple cylinder-based delivery systems.

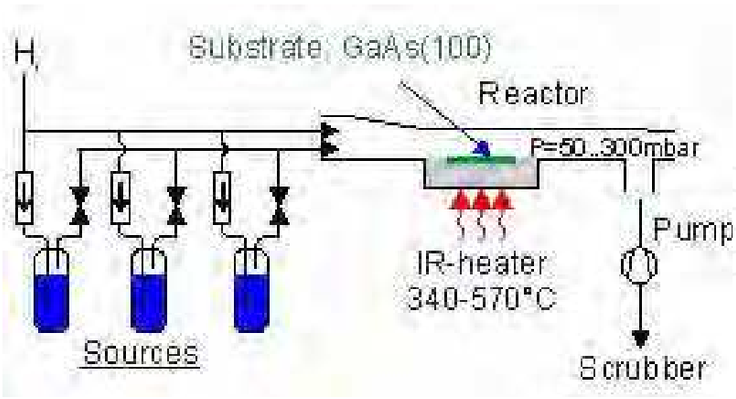

Fig. 5. Schematic view of a MOCVD reactor (Coleman, 1997).

MOCVD reactors consist of three major components: the reactor gas delivery system, the reaction chamber and the reactor safety infrastructure. The reactor delivery system or gas panel is a very clean, leak-free network of stainless-steel tubing, automatic valves and electronic mass flow controllers as shown in Fig. 6. Hydride delivery modules generally require a few valves and an electronic mass flow controller, since these sources are already provided as dilute, high pressure gases in gas cylinders. An important part of the main gas panel is the supply of carrier gases within a vent-run configuration.

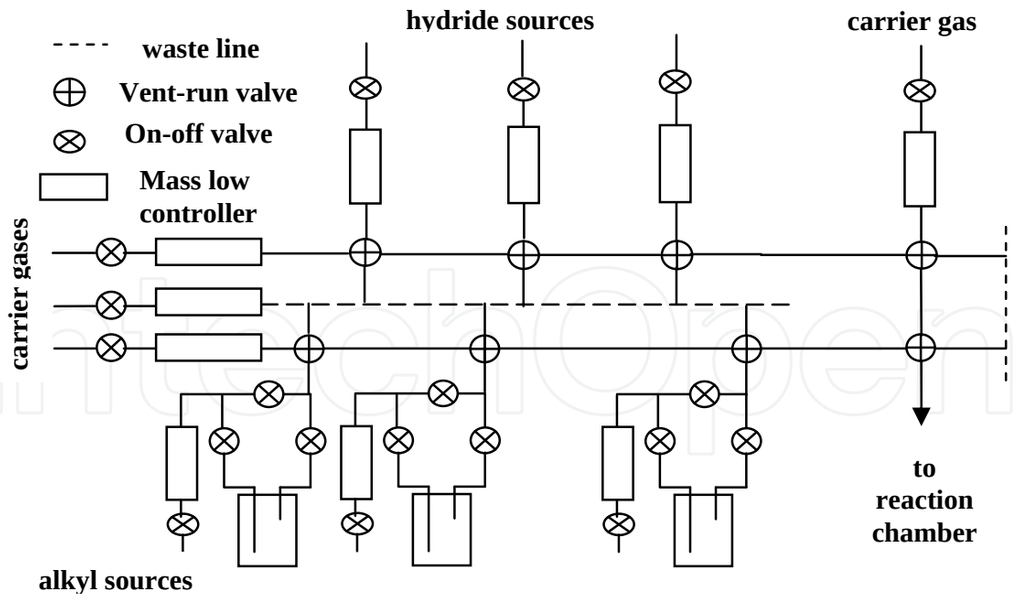

Fig. 6. Schematic diagram of MOCVD reactor delivery system gas panel, illustrating hydride delivery modules, alkyl delivery modules and the vent-run configuration (Coleman, 1997).

The reaction chamber is the vessel in which the source gases are mixed, introduced into a heated zone where an appropriate substrate is located, and the basic pyrolysis reactions take

place. There are two basic reaction-chamber geometries (Manasevit, 1968) commonly used for the MOCVD growth of optoelectronic materials, see Fig. 7.

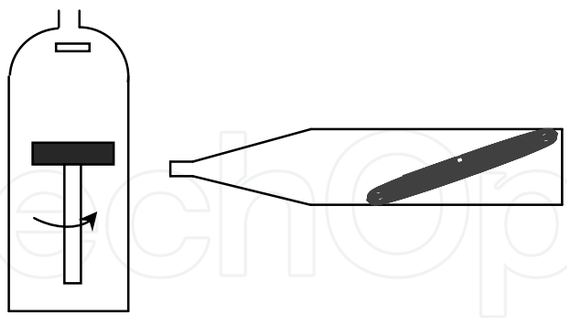

Fig. 7. Two common chamber geometry designs for MOCVD. (a) vertical (b) horizontal (Manasevit, 1968).

Both designs are cold-wall systems that reflect the basic pyrolysis nature of the process and make use of an indirectly heated (radio-frequency induction heated or infrared radiant heated) silicon carbide-coated graphited susceptor. The chamber itself can be quartz, stainless steel or quartz-lined stainless steel.

Safety is of paramount importance in the design and operation of MOCVD growth apparatus whether the sources used are hydride or not (Johnson, 1984). Hydrides pose the biggest risk because they are high-pressure toxic gases. The alkyls pose the next highest risk because, although they are toxic and pyrophoric, they are liquids and generally easier to handle. Ancillary risks include quartz reaction chambers (which are breakable), large volumes of explosive hydrogen gas, high temperatures, and the acids and solvents used for preparing for, and cleaning up after, a growth run. Handling these risks, falls into three categories applies equally well to all epitaxial growth process indeed to all semiconductor processing activities. The first is limited access, requires a higher level of authority and a correspondingly higher level of training. The second is training which required emergency-response situations such as hazardous-materials response and the third category is a hardware safety infrastructure. Automatic shutdown of source gases and a switch to inert purge gases should take place in the event of power failure when inadequate backup power is available.

The hydrodynamics of the reactor geometry play a key role in the nature of the process for MOCVD growth. In practical reactors, a large mismatch often exists between the inlet tube, which typically is a standard tube size of less than 10mm diameter and the characteristic dimensions of the reaction chamber. Thus, even in a relatively simple horizontal reaction chamber, the gas may have to travel well into the chamber before a simple parabolic profile stabilizes.

A heated zone is necessary to drive the pyrolysis reaction and provide for the desired materials deposition. The temperature gradient between the susceptor and the chamber ambient can be very large, often several hundreds of degrees Celsius. For example, the optimum MOCVD growth temperature for many III-V compounds and alloys falls in the range of 600-800 ^{o}C. Air or water cooling is often used to maintain the chamber walls at temperature close to room temperature.

The atomic force microscope (AFM) results of QW and QD InGaAs structure clearly show that the MOCVD reactor works so good, as shown in Fig. 8. Further more studies and more parameters should be taken for better characterization of the highly strained epilayer which is useful for quantum devices applications (Muhammad et al., 2007).

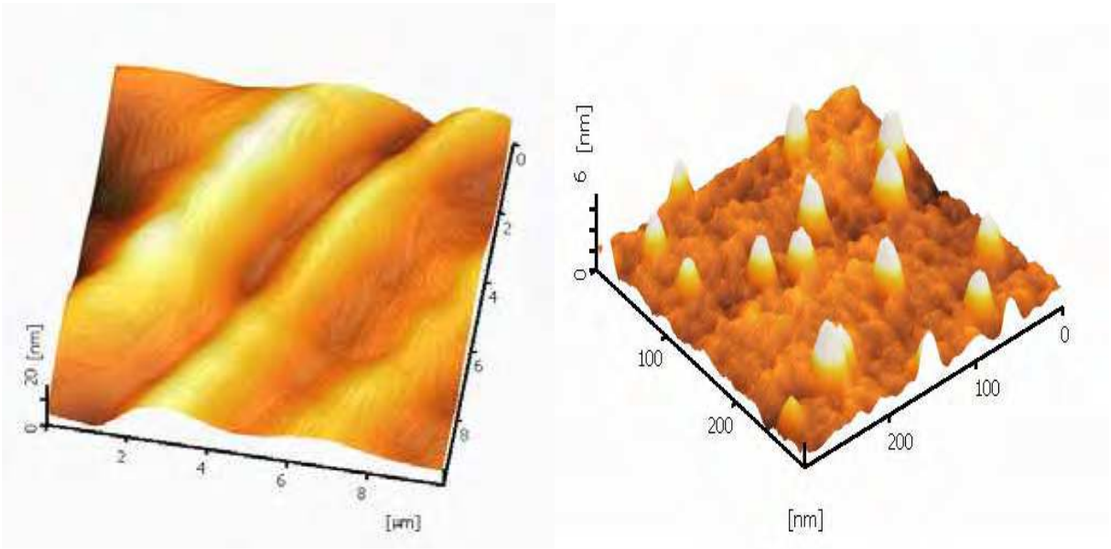

Fig. 8. AFM results of (a) Quantum well and (b) Quantum dot InGaAs on GaAs wafer (Muhammad et al., 2007).

By applying preceding conventional epitaxial crystal growth techniques, it is possible to gain precise orientation control during nanowire growth. The technique, vapor-liquid-solid epitaxy (VLSE), is particularly powerful in the controlled synthesis of high-quality nanowire arrays and single-wire devices. For example, ZnO prefers to grow along the [001] direction and readily forms highly oriented arrays when epitaxially grown on an a-plane sapphire substrate as shown in Fig. 9 (Pauzauskie & Yang; 2006).

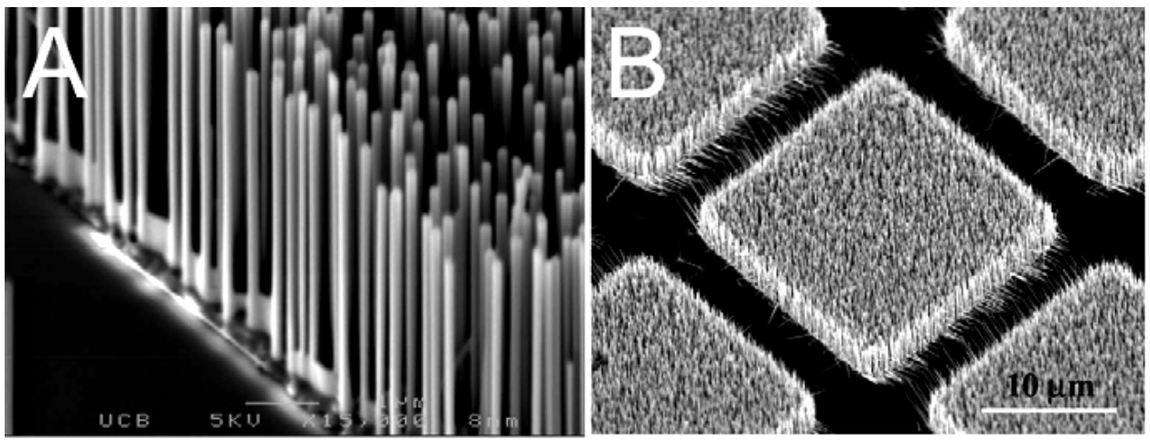

Fig. 9. Scanning Electron Microscope (SEM) images of (a) a [001] ZnO nanowire array on an a-plane sapphire wafer, and (b) [110] GaN nanowire arrays on (100) plane γ-LiAlO2 (Pauzauskie & Yang; 2006).

4. General principles of electroluminescent devices

To understand the physical meaning of the detection process, we must mention how light emitting and how we choose the layer structure of any device (Detector or source of light). Fig. 10 shows the layer structure and circuit diagram for a typical electroluminescent device. The device consists of several epitaxial layers grown on top of a thick crystal substrate. The epitaxial layers consist of a *p-n* diode with a thin active region at the junction. The diode is operated in forward bias with a current flowing from the *p-layer* through to the *n-layer* underneath. The luminescence is generated in the active region by the recombination of electrons that flow in from the *n-type* layer with holes that flow in from the *p-type* side (El_Mashade et al., 2003).

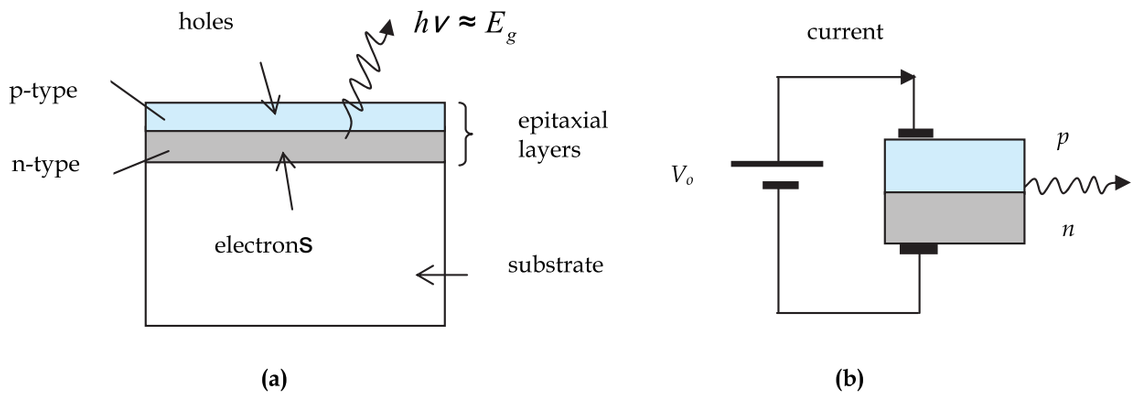

Fig. 10. (a) Layer structure and (b) circuit diagram for a typical electroluminescent device. The thin active region at the junction of the p-type and n-type is not shown, and the dimensions are not drawn to scale. The thickness of epitaxial layers will be only ~1μm, whereas the substrate might be ~500μm thick. The lateral dimensions of the device might be several millimetres (El_Mashade et al., 2003).

Any direct gap semiconductor can, in principle, be used for the active region, but in practice only a few materials are commonly employed. The main factors that determine the choice of the material are:

- The size of the band gap;
- Constraints related to lattice matching;
- The ease of p-type doping.

The first point is obvious: the band gap determines the emission wavelength. The second and third points are practical ones relating by which the way the devices are made. These are discussed further below.

These techniques are crucial to the successful growth of the high quality QIRPs structures described in the last section. The crystal growth conditions constrain the epitaxial layers to form with the same unit cell size as the substrate crystal. This means that the epitaxial layers will be highly strained unless they have the same lattice constant as the substrate, which meaning; we have 'lattice matching' between the epitaxial layers and the substrate. If this condition is not satisfied, crystal dislocations are likely to form in the epitaxial layers, which

would severely degrade the optical quality. Fig. 11 plots the band gap of a number of III-V materials used in electroluminescent devices against their lattice constant. The lattice constants of the commonly used substrate crystal are indicated at the top of the figure. The materials separate into two groups. On the right we have the arsenic and phosphorous compounds which crystallize with the cubic zinc blende structure, while on the left we have the nitride compounds which have the hexagonal wurtzite structure (El_Mashade et al., 2003).

x	y	E_g(eV)	λ_g(μm)
0	0	1.35	0.92
0.27	0.58	0.95	1.30
0.40	0.85	0.80	1.55
0.47	1	0.75	1.65

Table 1. Band gap energy E_g (eV) and emission wavelength λ_g(μm) for several compositions of the direct band gap quaternary III-V alloy $Ga_xIn_{1-x}As_yP_{1-y}$. The composition indicated all satisfy the lattice-matching condition for InP substrates, namely x~0.74y.

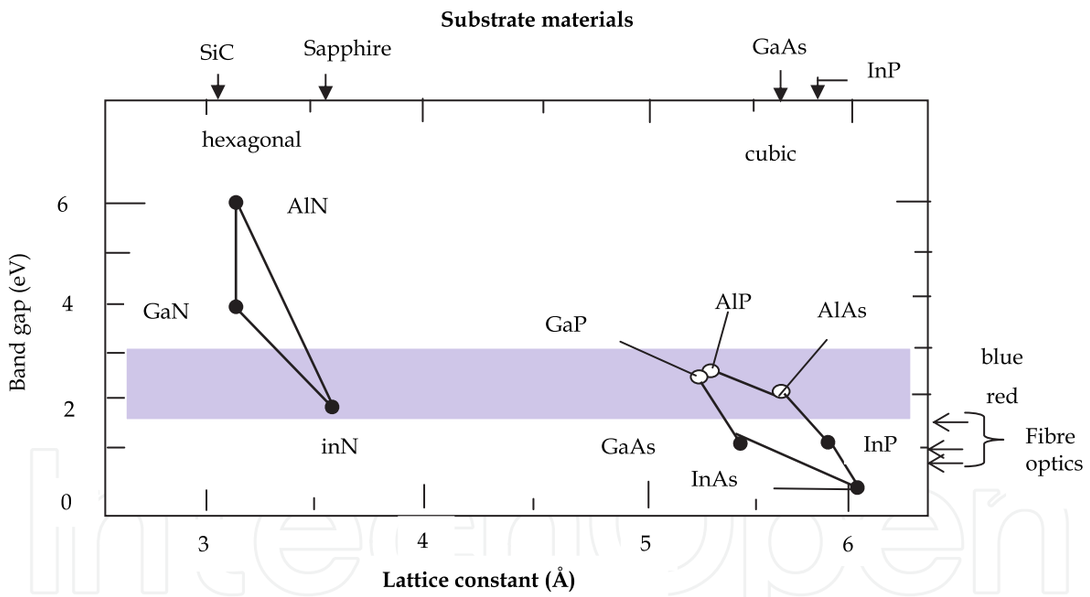

Fig. 11. Band gap of selected III-V semiconductors as a function of their lattice constant. The materials included in the diagram are the ones commonly used. The lattice constants of readily available substrate crystals are indicated along the top axis. The nitride materials on the left grow with the hexagonal wurtzite structure, whereas the phosphides and arsenides on the right have the cubic zinc blende structure (El_Mashade et al., 2003).

For many years, the optoelectronic industry has been mainly based on GaAs. GaAs emits in the infrared at 870 nm, and by mixing it with AlAs to form the alloy $Al_xGa_{1-x}As$, light emitters for the range 630-870 nm can be produced. Lattice-matched AlGaAs can easily be grown on GaAs substrates because of the convenient coincidence that the lattice constants of

GaAs and AlAs are almost identical. AlGaAs emitters are widely used in local area fiber optic networks operating around 850nm, and also for red LEDs. AlGaAs is an example of a 'ternary' alloy which contains three elements. 'quaternary' alloys such as $(Al_yGa_{1-y})_xIn_{1-x}P$ can also be formed. All of these arsenic and phosphorous alloys suffer from the problem that they become indirect as the band gap gets larger. This limits their usefulness to the red and near-infrared spectral range. Applications in the fiber optics industry require light emitting devices that operate around *1.3* μm and *1.55* μm. These are the wavelengths where silica fibers have the lowest dispersion and loss, respectively. Emitters for these wavelengths tend to be made from the quaternary alloy $Ga_xIn_{1-x}As_yP_{1-y}$. Lattice matching to InP substrates can be achieved if $x \sim 0.74y$. This allows a whole range of direct gap compounds to be made with emission wavelengths varying for 0.92 μm to 1.65 μm (Table 1) (El_Mashade et al., 2003).

P-type doping is difficult in wide band gap semiconductor because they have very deep acceptor levels. The high value of effective mass of hole, m_h* and the relatively small value of relative dielectric constant, $\varepsilon_{r,}$ increases the acceptor energies, and hence reduces the number of holes which are thermally excited into the valence band at room temperature. The low hole density gives the layer a high resistivity, which causes ohmic heating when the current flows and hence device failure. Nakamura's breakthrough came after discovering new techniques to activate the holes in p-type GaN by annealing the layers in nitrogen at 700C^o. In the last sections we will describe how the use of quantum well layers has led to further developments in the field of elecctroluminescent materials (Sze, 1981; Fox, 2001).

5. Photodetectors performance parameters

The fundamental mechanism behind the photodetcetion process is optical absorption. Consider a semiconductor slab, shown schematically in Fig. 12. If the energy $h\nu$ of incident photons exceeds the bandgap energy, an electron-hole pair is generated each time a photon is absorbed by the semiconductor. Under the influence of an electric field set up by an applied voltage, electrons and holes are swept across the semiconductor, resulting in a flow of electric current (Levine, 1993). The photocurrent I_p is directly proportional to the incident optical power P_{in}, that is,

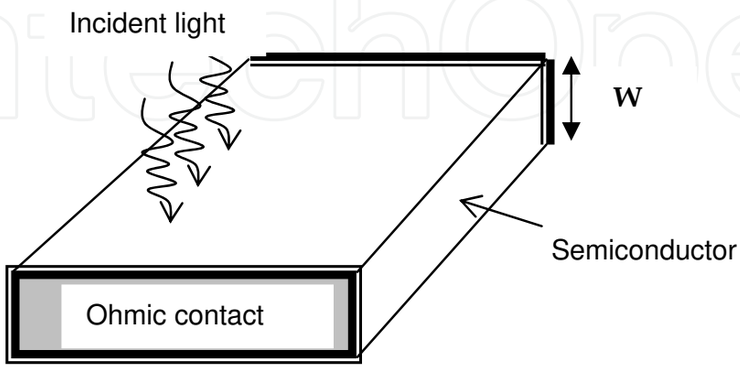

Fig. 12. A photoconductive detector

$$I_p = RP_{in} \tag{1}$$

where R is the responsivity of the photodetector (in unit of A/W). The responsivity R can be expressed in terms of a fundamental quantity η, called the quantum efficiency and defined as

$$\eta = \frac{electron-generation\quad rate}{photo-incidence\quad rate} = \frac{I_p / q}{P_{in} / h\upsilon} = \frac{h\upsilon}{q} R \tag{2}$$

where, $\hbar$ is the Plank's constant, q is the electron charge, υ is the light frequency.

substituting the value of I_p from Eq. (1) into Eq. (2)

i. The **Responsivity** R is given by:

$$R = \frac{\eta q}{h\upsilon} = \frac{\eta\lambda}{1.24} \tag{3}$$

where $\lambda = c/\upsilon$, c is the speed of light, and λ is expressed in micrometers. This relation shows that the responsivity of a photodetectors increases with the wavelength λ simply because the same current can be generated with photons of reduced energy. Such linear dependence on λ is not expected to continue forever, since eventually the photon energy becomes too small to generate electrons. In semiconductors this happens when the photon energy becomes less than the bandgap energy. The quantum efficiency η then drops to zero.

The dependence of η on λ enters through the absorption coefficient a. If the facets of the semiconductor slab in Fig. 12 are assumed to have an antireflection coating, the power transmitted through the slab of width W is $P_{tr} = \exp(-\alpha W)P_{in}$. The absorbed power is thus given by:

$$P_{abs} = P_{in} - P_{tr} = [1 - \exp(-\alpha W)]P_{in} \tag{4}$$

Since each absorbed photon creates an electron-hole pair,

ii. **The quantum efficiency** η is given by:-

$$\eta = P_{abs} / P_{in} = 1 - \exp(-\alpha W) \tag{5}$$

As expected, η becomes zero when $a=0$. On the other hand, η approaches 1 if $a\,W>>1$.

Photodetectors can be broadly classified into two categories: photoconductive and photovoltaic. A homogeneous semiconductor slab with ohmic contacts (see Fig. 12) acts as a simple kind of photoconductive detector. Little current flows when no light is incident because of low conductivity of semiconductor. Incident light increases conductivity through electron-hole generation, and allows current to flow in proportion to the optical power. Photovoltaic detectors operate through a built in electric field that opposes current flow in the absence of light. Electron-hole pairs generated through light absorption are swept across the device by the built-in electric field, resulting in a flow of electric current. Reverse biased p-n junctions fall in the category of photovoltaic detectors and are commonly used for light wave systems because of their high sensitivity and fast response.

Since infrared absorption due to intersubband transitions was first observed in multiple-quantum-well (MQW) structures, QWIPs and arrays based on this principle have become a

competitive infrared technology. The figure of merit used to evaluate the performance of most QWIPs is the specific *detectivity (D*),* which is a measure of the signal-to-noise ratio (SNR). In calculating the detectivity at a certain electrical frequency, the output noise current at this frequency must be known.

iii. The estimated dark current limited peak detectivity values, is defined as (Shen, 2000; Liu, 1992):

$$D^* = \frac{R\sqrt{A\Delta f}}{i_n} \quad cmHz^{1/2}/w \tag{6}$$

Where R is the responsivity, A is the area detector, i_n is the noise current can be estimated by $i_n^2 = 4eI_d g\Delta f$ Substituting in Eq. (6), the detectivity can be defined as:

$$D^* = \frac{R\sqrt{A\Delta f}}{\sqrt{4eI_d g}} \tag{7}$$

Theoretically, the dark current limited detectivity is proportional to $E_F \exp(-E_F / 2k_B T)$, which predicts a large change detectivity for change in the temperature.

6. Types of photodetectors

6.1 Photodiodes

A reverse-biased p-n junction consists of a region, known as the depletion region, that is completely devoid of free charge carriers and where a large built-in electric field opposes flow of electron from *n*- to *p*-side (and of holes from *p*- to *n*-side). When such a p-n junction is illuminated with light on one side, say the p-side (see Fig. 13), electron-hole pairs are created through absorption. Because of the large built-in electric field, electrons and holes generated inside the depletion region accelerate in opposite directions and drift to the *n*- and *p*-sides, respectively. The resulting flow of current is proportional to the incident optical power. Thus, a reverse-biased p-n junction acts as a photodetector and is referred to as the p-n photodiode. Considerable improvement in the performance of such photodiodes is possible through suitable modifications. Two such devices are known as the p-i-n photodiode and the avalanche photodiode (APD). This section starts with a discussion of simple p-n photodiodes and then considers p-i-n and APD devices (Zhao, 2006).

6.2 p-n photodiodes

Fig. (13- a) shows the structure of a p-n photodiode. The semiconductor structure device was based on a junctions formed between the same material with different doping, for example; p-type or n-type on GaAs, is known as homojunction. As shown in Fig. 13- b, incident light is absorbed not only inside the depletion region but also outside it. Photons absorbed inside the depletion region generate electron-hole pairs which experience a large electric field and drift rapidly toward the p- or n-side depending on the electric charge (Fig. 13- c). The resulting current flow constitutes the photodiode response to the incident optical power with Eq. (1).

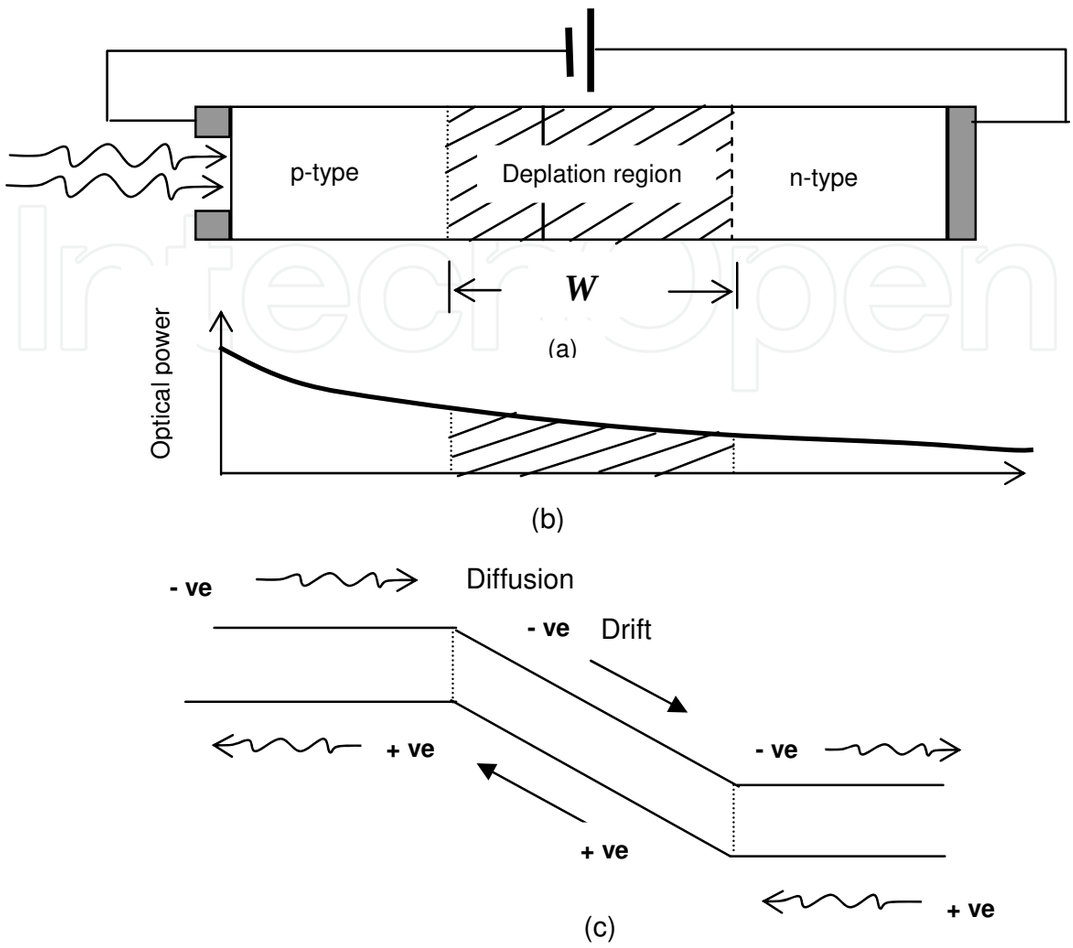

Fig. 13. (a) p-n photodiode and the associated depletion region under reverse bias. (b) Variation of optical power inside the photodiode. (c) Energy-band diagram showing carrier movement through drift inside the depletion region and through diffusion outside it (Zhao, 2006).

The response time is governed by the transit time. If W is the width of the depletion region and v_s is the average drift velocity, the transit time is given by (Fox, 2001):

$$\tau_{tr} = W / v_s \tag{8}$$

Typically, W~$10\mu m$, v_s=10^7 cm/s, and τ_{tr}~$100ps$. This value is small enough that p-n photodiodes are capable of operating up to bit rates of about 1Gb/s. Both W and v_s can be optimized to minimize τ_{tr}. The depletion-layer width depends on the acceptor and donor concentrations N_A and N_D, used to make the p-n junction and is given by (Sze, 1981):

$$W = [\frac{2\varepsilon}{q}(V_{bi} + V_o)(\frac{1}{N_A} + \frac{1}{N_D})]^{1/2} \tag{9}$$

where ε is the dielectric constant, V_{bi} is the built-in voltage, and V_o is the applied voltage. The value of V_{bi} depends on the semiconductor material and is $1.1V$ for GaAs. The velocity

v_s depends on the applied voltage but attains a maximum value (called the saturation velocity) in the range 5-10×10^{-6} cm/s, depending on the material used for the photodiode.

The limiting factor for p-n photodiodes is the presence of a diffusive component in the photogenerated current. The physical origin of the diffusive component is related to the absorption of incident light outside the depletion region. Electrons generated in the p-region have to diffuse to the depletion-region boundary before they can drift to the n-region; similarly, holes generated in the n-region must diffuse to the depletion-region boundary. Diffusion is an inherently slow process; carriers take a nanosecond or larger to diffuse over a distance of about *1μm*. Fig. 15 shows how the presence of diffusive component can distort the temporal response of a photodiode. In practice, the diffusion contribution depends on the bit rate and becomes negligible if the optical pulse is much shorter than the diffusion time. It can also be reduced by decreasing the widths of p- and n-regions and increasing the depletion region width so that most of incident optical power is absorbed inside it. This approach adopted for p-i-n photodiodes will be discussed next.

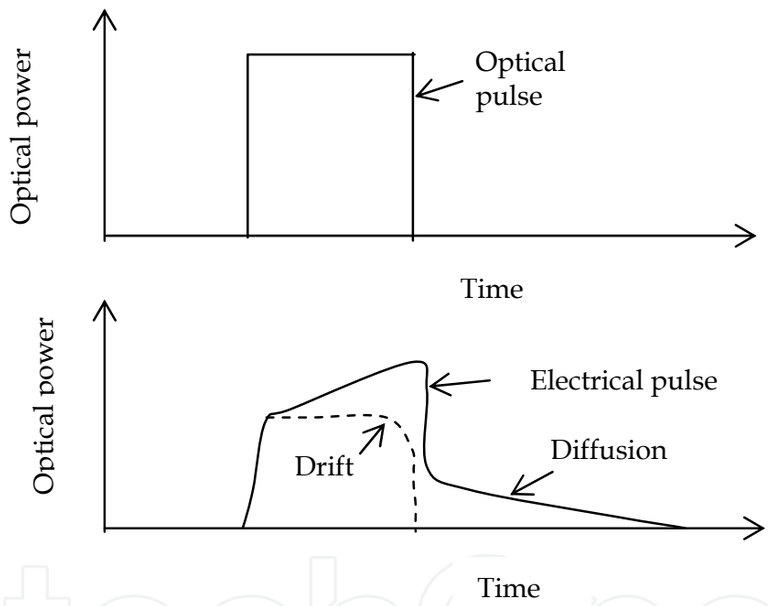

Fig. 14. Response of a p-n photodiode to a rectangular optical pulse when both drift and diffusion contribute to the detector current (Zhao, 2006).

6.3 p-i-n photodiodes

A simple way to increase the depletion-region width is to insert a layer of undoped (or lightly doped) semiconductor material between the p-n junctions. Since the middle layer consists of nearly intrinsic material, such a structure is referred to as the p-i-n photodiode (Zhao, 2006). Fig. (15-a) shows the device structure together with the electric field distribution inside it under reverse-bias operation. Because of the intrinsic nature of the middle layer, this layer offers a high resistance, and most of the voltage drop occurs across it. As a result, a large electric field exists in the middle of i-region. In essence, the depletion region extends throughout the i-region, and its width *W* can be controlled by changing the

middle layer thickness during fabrication. The main difference from the p-*n* photodiode is that the drift component of the detector current dominates over the diffusion component simply because most of the incident power is absorbed inside the i-region of the p-i-n photodiode. Since the depletion width *W* can be tailored in p-i-n photodiodes, a natural question is how large *W* should be. The optimum value of *W* depends on a compromise between responsivity and the response time. The responsivity can be increased by increasing *W* so that the quantum efficiency η approaches 100%. However, the response time also increases, as it takes longer for carriers to drift across the depletion region. For indirect-bandgap semiconductor such as *Si* and *Ge*, typically *W* must be in the range *20-50* μm to ensure reasonable quantum efficiency. The bandwidth of such photodiodes is then limited by slow response associated with a relatively long transit time *(> 200ps*). By contrast, *W* can be as small as *3-5μm* for photodiodes that use direct bandgap semiconductors such as InGaAs. The transit time for such photodiodes is in range τ_{tr}*=30-50ps* if we use v_s *=1×10*^{7}*cm/s* for the saturation velocity. Such values of τ_{tr} correspond to a detector bandwidth Δf*=3-5GHz* if we define the bandwidth as $\Delta f_t = (2\pi\tau_{tr})^{-1}$. Bandwidth as high as *20 GHz* have been achieved for optimized p-i-n photodiodes [6]. Even higher values are possible (*up to 70 GHz*) with a narrow i-region *(<1μm),* but only at the expense of a lower quantum efficiency and responsivity (Sze, 1981).

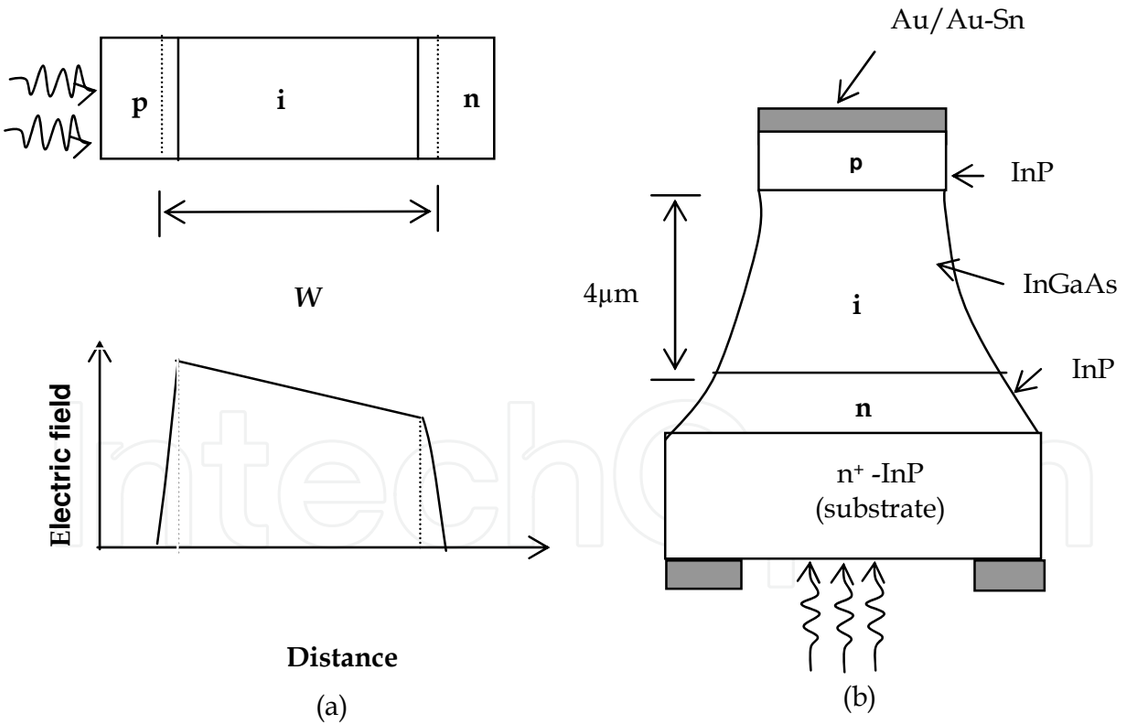

Fig. 15. (a) A p-i-n photodiode together with the electric field distribution inside various layers under reverse bias. (b) Design of an InGaAs p-i-n photodiode (Tucker et al., 1986).

The performance of p-i-n photodiodes can be considerably improved by using a double-heterostructure design. Similar to the case of semiconductor lasers, the middle i-type layer

is sandwithched between the p-type and n-type layers of a different semiconductor whose bandgap is chosen such that light is absorbed only in the middle i-layer. A p-i-n photodiode commonly used for lightwave applications uses InGaAs for the middle layer and InP for the surrounding p-type and n-type layers (Sze, 1981; Tucker et al., 1986). Fig. 15 -b shows such an InGaAs p-i-n photodiode. Since the band gap of InP is *1.35eV*, InP is transport for light whose wavelength exceeds *0.92 μm*. By contrast, the bandgap of lattice-matched InGaAs material is about *0.75 eV*, a value that corresponds to a cutoff wavelength of *1.65μm*. The middle InGaAs layer thus absorbs strongly in the wavelength region *1.3-1.6μm*. The diffusive component of the detector current is completely eliminated in such a heterostructure photodiode simply because photons are absorbed only inside the depletion region. The quantum efficiency η can be made almost 100% by using an InGaAs layer of several micrometers thick. The front facet is often antireflection-coated to minimize reflections. InGaAs photodiodes are quite useful for lightwave systems operating near *1.3-* and *1.55μm* wavelengths and are often used in optical receivers.

6.4 Avalanche photodiodes

All detectors require a certain amount of minimum current in order to operate reliably. The current requirement translates into a minimum power requirement through $P_{in}=I_p/R$ (see Eq. (1)). Detectors with a large responsivity R are preferred, since they require less optical power. The responsivity of p-i-n photodiodes is limited by Eq. (3) and takes its maximum value $R = q / h\nu$ for $\eta=1$. APDs can have much larger values of R, as they are designed to provide an internal current gain in a way similar to photomultiplier tubes. They are generally used in optical communication systems for which the amount of optical power that can be spared for the receiver is limited. The physical phenomenon behind the internal current gain is known as impact ionization (Stillman & Wolfe; 1977; Melchior, 1977).

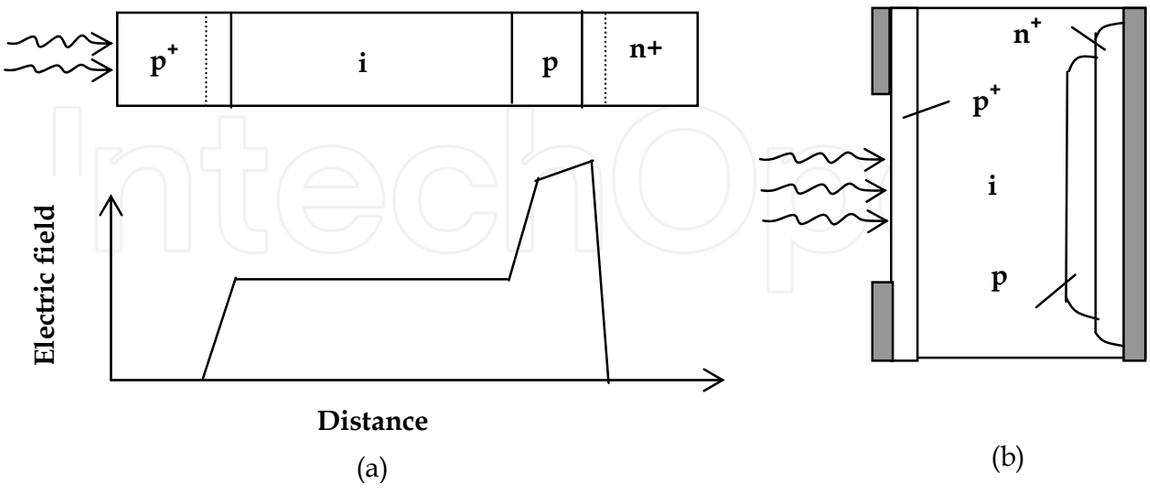

Fig. 16. (a) an APD together with the electric-field distribution inside various layer under reverse bias. (b) Design of a silicon reach-through APD [42, 43]

Under certain conditions, an accelerating electron can acquire sufficient energy to generate a new electron–hole pair. The energetic electron gives a part of its kinetic energy to another electron in the valance band that ends up in the conduction band, leaving behind a hole. The net result of impact ionization is that a single primary electron, generated through absorption of photon, creates many secondary electrons and holes, all of which contribute to the photodiode current. Of course, the primary hole can also generate secondary electron-hole pairs that contribute to the current. The generation rate is governed by two parameters, a_e and a_h, known as the impact-ionization coefficients of electrons and holes, respectively. The numerical value of these coefficients depends on the semiconductor material and on the electric field that accelerates electrons and holes. Values on the order of $1\times10^4\ cm^{-1}$ are obtained for an electric field in the range $2\text{-}4\times10^5\ V/cm$. Such large fields can be realized by applying a high voltage ($>100V$) to the APD.

APDs differ in their design from that of p-i-n photodiodes mainly in one respect. An additional layer is added through which secondary electron-hole pairs are generated by impact ionization. Fig. 16-a shows the APD structure together with the variation of electric field in various layers. Under reverse bias, a high electric field exists in the p-type layer sandwiched between i-type and n^+-type layers. This layer is referred to as the gain region or the multiplication region, since secondary electron-hole pairs are generated here through impact ionization. The i-layer still acts as a depletion region in which most of the incident photons are absorbed and primary electron-hole pairs are generated. Electrons generated in the i-region cross the gain region and generate secondary electron-hole pairs responsible for the current gain. The current gain or the multiplication factor M is given by (Stillman & Wolfe; 1977; Melchior, 1977):

$$M = \frac{1 - k_A}{\exp[-(1 - k_A)\alpha_e d] - k_A} \tag{10}$$

where d is the thickness of the gain region, $k_A = \alpha_h / \alpha_e$. The APD gain is quite sensitive to the ratio of the impact-ionization coefficients. Where $\alpha_h = 0$ so that only electrons participate in the avalanche process, $M = \exp(\alpha_e d)$, and the APD gain increases exponentially with d. On the other hand, when $\alpha_h = \alpha_e$ so that $k_A = 1$ in Eq. (10), $M = (1 - \alpha_e d)^{-1}$. The APD gain then becomes infinite for $\alpha_e d = 1$, a condition known as the avalanche breakdown. Although higher APD gain can be realized with a smaller gain region when $\alpha_e and \alpha_h$ are comparable, the performance is better in practice for APDs in which either $\alpha_e >> \alpha_h$ or $\alpha_h >> \alpha_e$, so that the avalanche process is dominated by only one type of charge carrier. Because of the current gain, the responsivity of APD is enhanced by the multiplication factor M and is given by

$$R_{APD} = MR = M(\eta q / h\nu) \tag{11}$$

It should be mentioned that the avalanche process in APDs is intrinsically noisy and results in a gain factor that fluctuates around the average value. The intrinsic bandwidth of an APD depends on the multiplication factor M. This is easily understood by noting that the transit time τ_{tr} for an APD is no longer given by Eq. (8) but increases considerably simply because generation and collection of secondary electron-hole pairs take additional time. A particularly useful design is known as reach-through APD (see Fig. 16-b) because the

depletion layer reaches to the contact layer through the absorption and multiplication regions. It can provide high gain ($M \approx 100$) with low noise and relatively large bandwidth.

6.5 Advanced APD structures

It is difficult to make high-quality APDs that operate in the wavelength range *1.3-1.6μm* that is of interest for most lightwave systems. A commonly used material is InGaAs (lattice-matched to InP) with a cutoff wavelength of about *1.65μm*. However, the impact-ionization coefficients α_e *and* α_h for InGaAs are comparable in magnitude (Campbell, 1983). As a result, the bandwidth is considerably reduced, and the noise is also high. Furthermore, because of a relatively narrow bandgap, InGaAs undergoes tunneling breakdown at electric fields of about 1×10^5 *V/cm*, a value that is below the threshold for avalanche multiplication. This problem can be solved in heterostructure APDs by using an InP layer for the gain region because quite high electric fields *(*$>5\times10^5$ *V/cm*) can exist in InP without tunneling breakdown. Since the absorption region (i-type InGaAs) and the multiplication region (n-type InP layer) are separate in such a device, this structure is known as separate absorption and multiplication *(SAM)* APD. Since $\alpha_h > \alpha_e$ for InP, the APD is designed in such away that holes initiate the avalanche process in an *n-type* InP layer, and K_A is defined as $K_A = \alpha_e / \alpha_h$. Fig. (17- a) shows a mesa-type SAM APD structure. One problem with a SAM APD is related to the large bandgap difference between InP (E_g=*1.35 eV*) and InGaAs (E_g =0.75 *eV*). Because of a valence-band step about *0.4 eV*, holes generated in the InGaAs layer are trapped at the heterojunction interface and are considerably slowed before they reach to the multiplication region (InP layer). Such an APD has an extremely slow response and relatively small bandwidth. This problem can be solved by using another layer between the absorption and multiplication regions whose bandgap is intermediate to those of InP and InGaAs. The quaternary material InGaAsP, the one used for semiconductor lasers, can be tailored to have a bandgap anywhere in the range *0.75-1.35 eV* and is ideal for this response. It is even possible to grade the composition of InGaAsP over the distances of roughly *10-100 nm*. Such APDs are called SAGM APDs, where SAGM indicates separate absorption, grading, and multiplication regions.

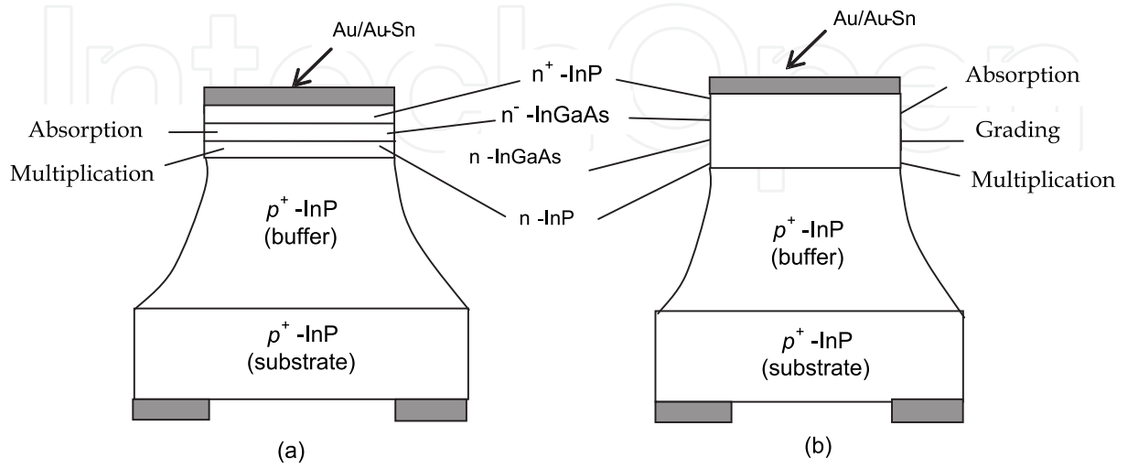

Fig. 17. Design (a) a SAM APD and (b) a SAGM APD (Kasper & Campbell, 1987; Tarif, 1991).

Fig. 17- b shows the design of an InGaAs APD with the SAGM structure. The use of InGaAsP grading layer improves the bandwidth considerably. This device exhibited a gain-bandwidth product of about 70 GHz for *M>12*. Values up to *100GHz* have been demonstrated by using a "charge region" between the grading and multiplication regions (Kasper & Campbell, 1987; Tarif, 1991).

A different approach to the design of high-performance APDs is provided by multiquantum-well (MQW) or superlattice structure (Tarif, 1991) [46]. The major limitation of SAM APDs results from nearly equal values of α_e and α_h resulting in K_A=*0.7*. A MQW design offers the possibility of reducing the value of K_A from the bulk value of nearly unity. The absorption and multiplication regions in MQW APDs alternate and consist of thin layers (~10nm) of different bandgap semiconductor materials. In this sense, the APD design is quite similar to MQW semiconductor lasers except that the device parameters are optimized to result in a lower value of K_A. This approach was first demonstrated for GaAs/AlGaAs MQW APDs and resulted in a considerable enhancement of the electron impact-ionization coefficient (Capasso, 1985). It is less successful for InGaAs/InP material system. Progress has been made through the so-called staircase APDs, in which the InGaAsP layer is compositionally graded to form a sawtooth kind structure in the energy-band diagram that looks like a staircase under reverse bias (Capasso, 1985). Another technique for making high-speed APDs uses alternate layers of InP and InGaAs layers for the grading region (Capasso, 1985). However, the ratio of widths of the InP to InGaAs layers varies from zero near the absorbing region to almost near the multiplication region. Since the effective bandgap of a quantum well depends on the quantum-well width (InGaAs layer thickness), a graded "pseudo-quaternary" compound is formed as a result of variation in the layer thickness. The performance of InGaAs APDs has improved considerably as a result of many such advances.

6.6 UV photodetectors

With their direct bandgap tunable from 200 to 365 nm, $Al_xGa_{1-x}N$ alloys are among the best candidates for ultraviolet (UV) photodetectors. Applications for such devices include solar UV detection, visible blind detection, missile warning, space communication and flame sensing, see Fig. 18 (Norbert & Jurgen,2005; NASA, 1999; Hsueh et al.; 2007). Actually, photomultiplier tube light detectors are the most efficient devices for flame sensing, however, they suffer from their high price, a limited lifetime of 1 to 2 years, a large size and the need of high voltage power supply. For utilization under room light or solar light, the UV flame detector should be able to selectively sense the flame wavelength below 280 nm, meaning that it should be able to detect light intensities below 1 nW/cm^2 with a rejection ratio between UV and visible light of six orders of magnitude. Also, the flame detector should be able to operate in a high temperature field and a response speed on the order of few *ms* is required for safety switch applications. Thanks to the use of a low-temperature-deposited buffer layer and the realization of p-type GaN (Norbert & Jurgen, 2005), the nitride research encounters a vast development. Achievement of photoconductors, photodiodes and phototransistors has been reported. However, for low-intensity detection a high photocurrent on dark current ratio (PC/DC) is needed in order to avoid misdetection, especially for a device operating in a wide range of temperatures. Photocurrent values close to the expected level have been reported, however, for dark current level, the reported results are still far from theoretical limit. For Schottky, *p-n* or *p-i-n* photodiodes, one of the origins of high leakage current was attributed to the high level of threading dislocations (10^9 to 10^{10} cm^{-2}) present in the current GaN epilayer. Recently, it was reported that the insertion of low-temperature-deposited GaN or AlN inter-layers between

high-temperature-grown GaN layers reduced the threading dislocations. The insertion of a high quality intrinsic layer in devices such as PIN photodiodes or phototransistors is believed to be one of the key points to improve the performance of those UV photodetectors (Pernot et al., 1999). Comparison of different types of UV photodetectors is denoted in table 2 (Waleker et al., 2000).

Photodetector type	Advantages	Disadvantages	Challenges
photoconductors	-Easy to fabricate -Internal photoelectric gain	-Low speed -Large dark current -Large Johnson noise	-Interdigitated patterns require enhanced resolution
p-n or p-i-n photodiodes	-Low or zero dark current -High speed -High impedance (good for FPA readout circuitry) -Compatible with planar processing technology (for FPA) -For p-i-n photodiodes, easy optimization of quantum efficiency and speed with I layer	-Speed is limited by minority carried diffusion time and storage time -Speed and quantum efficiency trade-off	-Etching is necessary to expose various layers -Ohmic contacts necessary to both n- and p-type material
MSM or Schottky photodiodes	-High efficiency -High speed -Easy to fabricate	-Require high absorption coefficient -No-sharp cut-off (below bandgap response) -Front side illumination needed	-Schottky contact is needed

Table 2. Comparison of different types of UV photodetectors (Waleker et al., 2000).

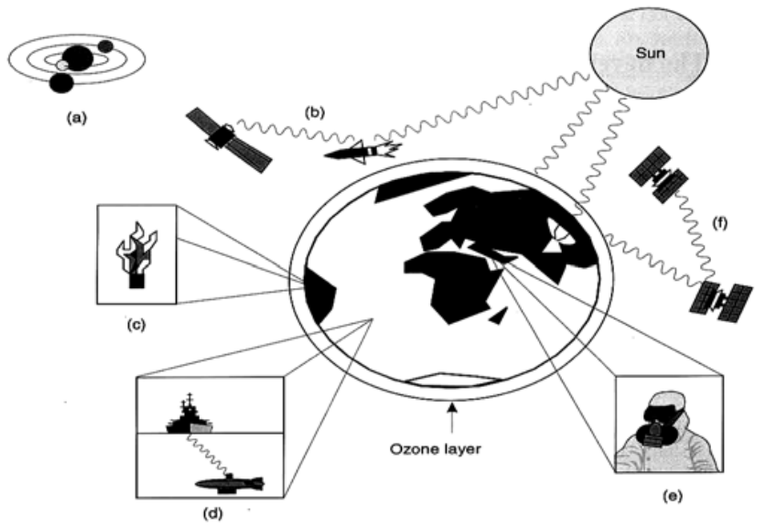

Fig. 18. Applications for UV photodetectors: (a) UV astronomy, (b) solar blind detectors, (c) flame detection and engine monitoring (d) underwater UV communications, (e) chemical/ biological battlefield reagent detectors, (f) space communications secure from Earth (Pernot et al., 1999).

6.6.1 Future and recent advances of UV photodetectors

Many astronomical objects produce orders of magnitudes more photon fluxes at optical wavelengths than they do in the vacuum UV. In order to eliminate this huge background contribution and substantial source of noise solar-blind detector and imaging systems are required. A comprehensive study of UV imaging detectors is given by (Norbert & Jurgen, 2005). Several specific detector types can be used for vacuum UV astronomy in the future, multidimensional detectors, semi-conductive array (e.g. CCDs) and microchannel plate detector (MCP). Recent research teams are studied the UV nanowires. They found that the conductivity of the ZnO nanowires was very sensitive to UV light. Very recently, researchers reported the growth of vertical, well aligned ZnO nanowires on ZnO :Ga and TiN buffer layers by reactive evaporation Hsueh et al.; 2007).

The further development of technologies for this detector is the basis to enhance the performance for UV applications. The current technology can be classified in two categories: Solid-state devices based on silicon or wide bandgap semiconductors and photoemissive devices, coupled with a gain component and an electron detector. The detective quantum efficiencies (DQE) for various UV detectors as MCPs, CCDs, Electron-Bombarded CCDs and for the expected DQEs for future A1GaN solid-state sensors are shown in Fig.19.

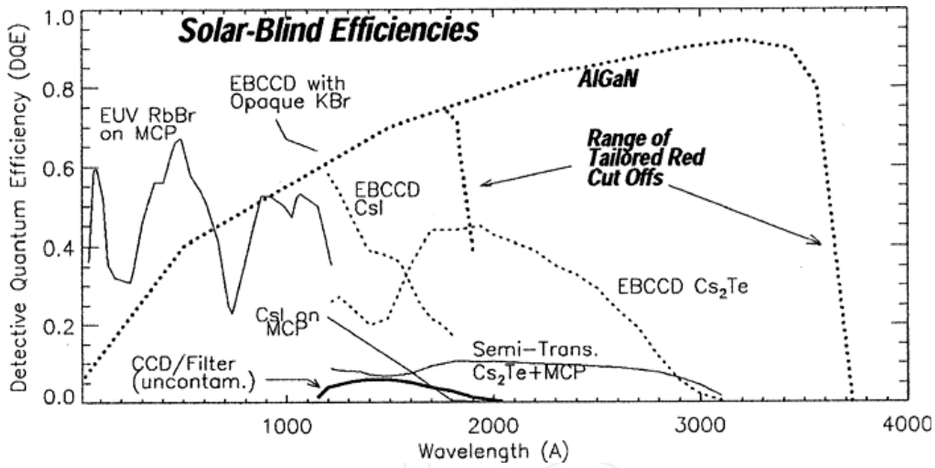

Fig. 19. Solar-blind detective quantum efficiencies obtained by various UV detector adopted (Norbert & Jurgen, 2005).

7. Quantum IR photodetectors

Mercury cadmium telluride (HgCdTe), which works at both medium and long IR wavelengths, is one of the most common materials used in photo detectors; however its limitation is the need to use a cryostat to manage heat generated in the device (www.nanoforum.org, 2007). Here, the focusing will be directed to the quantum IR detectors.

7.1 Idea of nanotechnology devices - Quantum confined structures

In this section, it will be given an overview of the optical properties of quantum confined semiconductor structures. These are artificial structures in which the electrons and holes are confined in one or more directions (Fox, 2001; www.nanoforum.org, 2007).

The optical properties of solids do not usually depend on their size. Ruby crystal, for example, have the same red colour irrespective of how big they are. This statement is only true as long as the dimensions of the crystal are large. If we make very small crystals, then the optical properties do in fact depend on the size. A striking example of this is semiconductor doped glasses. These contain very small semiconductor microcrystals within a colourless glass host, and the colour of the filter can be altered just by changing the size of the crystals.

The size dependence of the optical properties in very small crystals is a consequence of the quantum confinement effect. The Heisenberg uncertainty principle tells us that if we confine a particle to a region of the x axis of length Δx, then we introduce an uncertainly in its momentum given by:

$$\Delta p_x \sim \frac{\hbar}{\Delta x} \tag{12}$$

where $\hbar$ is the Plank's constant.

If the particle is otherwise free, and has a mass m, the confinement in the x direction gives it an additional kinetic energy of magnitude

$$E_{confinement} = \frac{(\Delta p_x)^2}{2m} \sim \frac{\hbar^2}{2m(\Delta x)^2} \tag{13}$$

This confinement energy will be significant if it is comparable to or greater than the kinetic energy of the particle due to its thermal motion in the x direction. This condition may be written:

$$E_{confinement} \sim \frac{\hbar^2}{2m(\Delta x)^2} > \frac{1}{2} K_B T \tag{14}$$

And tells us that quantum size effects will be important if

$$\Delta x \sim \sqrt{\frac{\hbar^2}{m K_B T}} \tag{15}$$

This is equivalent to saying that Δx must be of the same order of magnitude as the de Broglie wavelength $\lambda_{deB} \equiv p_x / \hbar$ for the thermal motion. The criterion given in Eq. (15) gives us an idea of how small the structure must be if we are to observe quantum confinement effects. For an electron in a typical semiconductor with $m^*_e = 0.1 m_o$ at room temperature, we find that we must have $\Delta x \sim 5nm$. Thus, a 'thin' semiconductor layer of thickness 1μm is no thin by the standards *of the electrons*. It is in fact a bulk crystal which would not exhibit any quantum size effects. To observe quantum size effects we need thinner layers. Table 3 summarizes the three basic types of quantum confined structures that can be produced. The structures are classified as to whether the electrons are confined in one, two or three dimensions. These structures are respectively called:

- quantum wells (1-D confinement);
- quantum wires (2-D confinement);
- quantum dots (3-D confinement).

Table 3 also lists the number of degrees of freedom associated with the type of quantum confinement. The electrons and holes in bulk semiconductors are free to move within their respective bands in all three directions, and hence they have three degrees of freedom. The electrons and holes in a quantum well, by contrast, are confined in one direction, and therefore only have two degrees of freedom. This means that they effectively behave as two-dimensional (2-D) materials. Similarly, quantum wire structures have 1-D physics, while quantum dots have '0-D' physics. This last point means that the motion of the electrons and holes is quantized in all three dimensions, so that they are completely localized to the quantum dot.

structure	Quantum confinement	Number of free dimensions
Bulk	none	3
Quantum well/superlattice	1-D	2
Quantum wire	2-D	1
Quantum dot/box	3-D	0

Table 3. Number of degree of freedom tabulated against the dimensionality of the quantum confinement.

The very small crystal dimensions required to observe quantum confinemt effect have to be produced by special techniques.

- Quantum well structures are made by techniques of advanced epitaxial crystal growth.
- Quantum wire structures are made by lithographic patterning of quantum well structures, or by epitaxial growth on patterned substrates.
- Quantum dots structures can be made by lithographic patterning of quantum well or by spontaneous growth technique.

Epitaxial techniques are very versatile, and they allow the growth of a great variety of quantum well structures as described in the first subsection of techniques of fabrications. Fig. (20-b) shows one such variant derived from the single well structure shown in Fig. (20-a). The crystal consists of a series of repeated GaAs quantum wells of width d separated from each other by AlGaAs layers of thickness b. This type of structure is either called a multiple quantum well (MQW) or a superlattice, depending on the parameters of the system. The distinction depend mainly on the value of b. MQWs have b values, so that the individual quantum wells are isolated from each other, and the properties of the system are essentially the same as those of single quantum wells. But in the case of a superlattice the values of b and d are equal. They are often used in optical applications to give a usable optical density. It would be very difficult to measure the optical absorption of a single $10nm$ thick quantum well, simply because there is so little to absorb the light. By growing many identical quantum wells, the absorption will increase to a measurable value (Levine, 1993).

7.2 Comparison between long wavelength photodetectors

An important application of detectors is in the area of the detection of long wavelength radiation (λ ranging from $5\text{-}20\mu m$). If a direct band to band transition is to be used for such detectors, the bandgap of the material has to be very small. An important material system in which the bandgap can be tailored from 0 to $1.5\ eV$ is the $HgCdTe$ alloy. The system is widely

used for thermal imaging, night vision application, etc. However, the small bandgap *HgCdTe* is a very "soft' material which is very difficult to process. Thus the device yield is rather poor. The quantum well intersubband detector offers the advantages of long wavelength detection using established technologies such as the GaAs technology (Piotrowski, 2004).

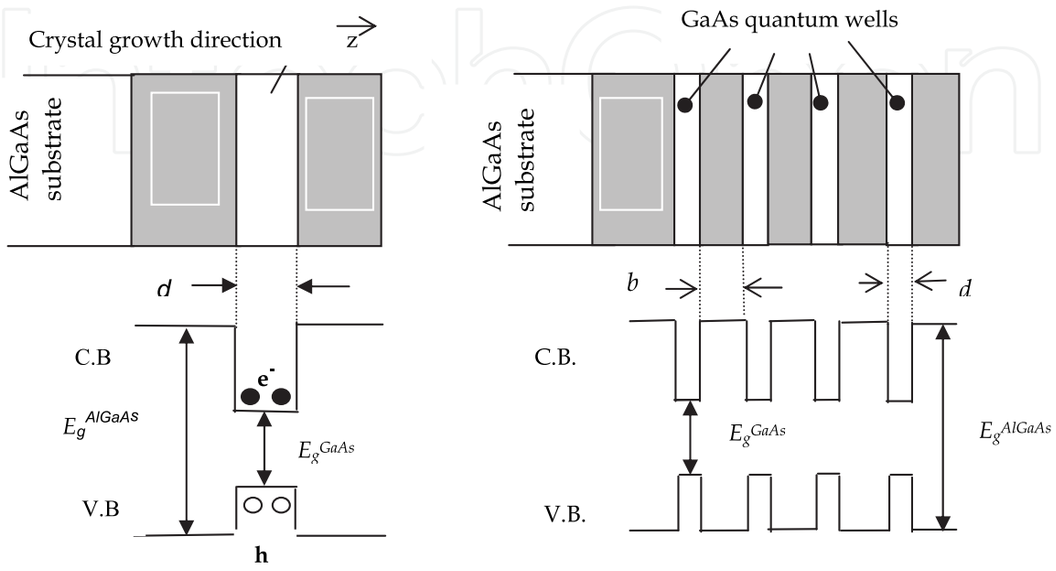

Fig. 20. (a) Schematic diagram of a single GaAs/AlGaAs quantum well. The quantum well is formed in the thin GaAs layer sandwiched between AlGaAs layers which have a larger bandgap. The lower half of the figure shows the spatial variation of the conduction band (C.B.) and the valence band (V.B.). (b) Schematic diagram of GaAs/AlGaAs multiple quantum well (MQW) or superlattice structure. The distinction between an MQW and a superlattice depends on the thickness b of the barrier separating the quantum wells (Levine, 1993).

In Fig. 21, we show a quantum well which is doped so that the ground states has a certain electron density and the excited state is unoccupied. When a photon with energy equal to the intersubband separation impinges upon the quantum well, the light is absorbed and the ground state electron is scattered into the excited state. For the absorption process to produce an electrical signal, one must have the following conditions satisfied:

1. The ground state electrons should not produce a current. If this is not satisfied, there will be a high dark current in the detector. The electrons in the ground state carry current by thermionic emission over the band discontinuity. At low temperatures this process can be suppressed. Now, there are many methods to obtain a high-operating-temperature infrared Photodetectors as in (Piotrowski & Rogalski, 2007).
2. It should be possible to extract the excited state electrons from the quantum well so that a signal can be produced. The excited electron state should, therefore, be designed to be near the top of the quantum well barrier, so that the excited electrons can be extracted with ease by an applied electric field.

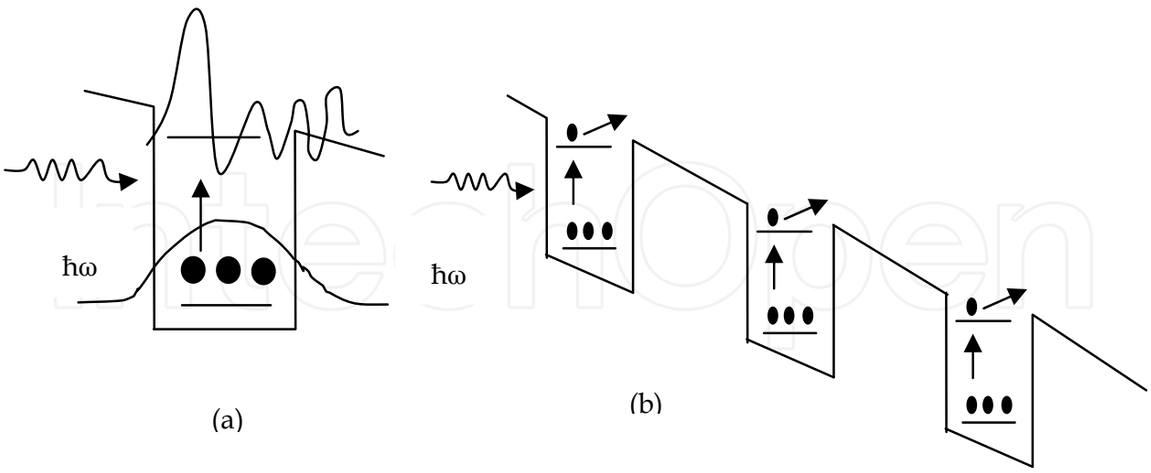

Fig. 21. (a) A schematic of the electron wave function in the ground state and the excited state. The photon causes transitions to the excited state from where the electrons are collected are shown in (b)

Band to band absorption detectors	Quantum well intersubband detectors
Narrow bandgap materials are "soft" and difficult to process. Therefore, device yield is poor	Established GaAs or InP based technologies can be used to produce high yield devices.
Dark current can be low at low temperatures, since an undoped material is used in the active region.	Dark current is usually high, since there are free carries in the quantum well regions.
	In the conduction band, quantum wells, vertical incident light is not absorbed.
Vertical imaging can be done	Mirrors have to be used, corrugated QW, or valence band quantum wells have to be used.
It is difficult to fabricate tunable detectors	Tunability can be achieved by altering the quantum well parameters.

Table 4. Comparison of the band to band and intersubband detectors for long wavelength detection

In the case of quantum well, the light is absorbed only if it is incident z-polarized. Here z is the quantum well growth direction. Thus, for vertical incidence, there is no absorption. This is an important drawback for such detectors. One way to overcome this problem is to use etched mirrors on the surface to reflect vertically incident light so that it has a z-polarization. Another way to avoid this is to use the intersubband transitions in the valence band where, due to the mixed nature of the HH and LH states, the z-polarization rule is not valid. However, the poor hole transport properties and the difficulty in reducing the dark current reduce the detector performance.

Quantum wire and quantum dot IR photodetectors overcome this problem as they are response to the normal incident IR rays (Nasr, 2009; Nasr et al., 2009; Nasr, 2008). In Table 4, a comparison of the band to band and intersubband detectors for long wavelength detection is shown (El_Mashade, 2003).

Fig. 22 shows the transition of electron in conduction band of QWIPs and each of photocurrent and dark currents. The inset shows a cross-section transmission electron micrograph of a QWIP sample (Gunpala et al., 2001).

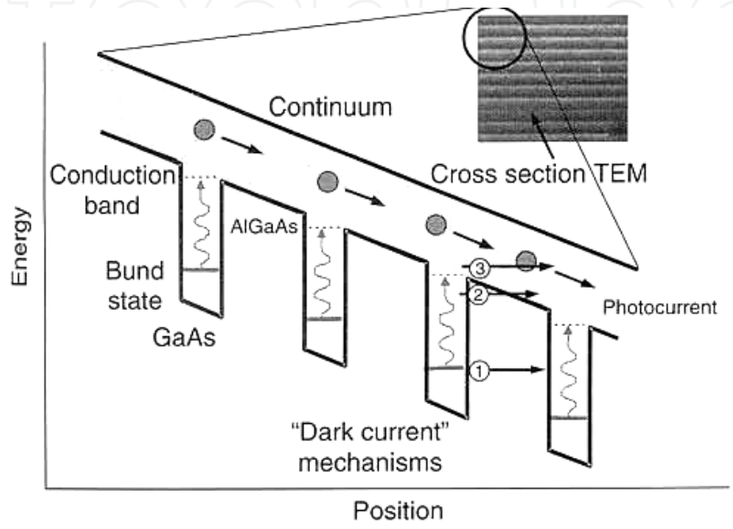

Fig. 22. Schematic diagram of the conduction band in a bound-to-quasibound QWIP in an externally applied electric field. Absorption of IR photons can photoexcite electrons from the ground state of the quantum well in the continuum, causing a photocurrent. Three dark current mechanisms are also shown: ground state tunneling (1); thermally assisted tunneling (2); and thermionic emission (3). The inset shows a cross-section transmission electron micrograph of a QWIP sample (Gunpala et al., 2001).

7.3 Quantum dot and wire infrared photodetectors

To eliminate the limitations of QWIP detectors, there has been significant interest in IR detectors with lower dimensions such as quantum wires (QR) (2-D) and quantum dots (QD) (3-D) (Das & Singaraju, 2005). The use of quantum wires and quantum dots for IR detection provides many advantages. From these advantages, first one, the sensitivity to normal incident IR. Second one, higher optical gain provided by QDIPs and QRIPs. Hence, the life time of the excited states in the QDs is expected to be longer arisen reduced capture probability due to the phonon bottleneck and formation of repulsive potential barriers by charged QRs or QDs. Third, The discreteness of the QR and QD energy spectrum which lead to expected IR wide band covering (long, medium, short IR region) (Nasr & El_Mashade, 2006; Phillips et al., 1999). Although of these strengths, there are drawbacks. The major one is a high value of dark current obtained as illustrated in theoretical and experimental results (Nasr et al., 2006; Ryzhii et al., 2000). In a previous work, we declared that QRIPs gives a smaller and acceptable values of dark current compared with QDIPs (Nasr & El_Mashade, 2006). This opens the way to overcome mentioned problem (Nasr, 2007).

The main features of operation of (QDIP) in conduction band are illustrated into Fig. (23-a) and can be summarized to the following:

1. Thermo- and photoexcition of electrons from bound states in QDs into continuum states,
2. Capture of mobile electrons into QDs (transition from continuum into bound states),
3. Transport of mobile electrons between the potential "hills" formed by charged QDs,
4. Injection of extra electrons from the emitter contact because of the redistribution of the potential in the QDIP active region caused by the change in the charges accumulated by QDs,
5. Collection of the excited and injection electrons by the pertinent contact.

The main features that differentiate QDIPs from QWIPs are associated with the discreteness of the QD energy spectrum leading to a dependence of the thermoactivation energy on the following (Ryzhii & Khmyrova, 2001):

The QD sizes, Strong sensitivity to normally incident radiation, phonon bottleneck effect (or similar effects) in the electron capture, and limitations imposed on the QD filling by the Pauli principle, the existence of the passes for mobile electrons between QDs, the activation character of the electron capture due to the repulsive potential of charge QDs and thermionic nature of the injection (Nasr & El_Mashade, 2006).

In the case of quantum wire IR photodetectors, The QRIPs under illumination by infrared radiations causes the photoexcitation of QRs because of the electron transitions from the bound states in QRs into the continuum states above the inter-QR barriers, the principle of QRIPs operation is shown in Fig. (23-b) (Nasr, 2007; Ryzhii & Khmyrova, 2001; Maksimović, 2003). The device structure is formed from quantum wires active layer separated by barrier layer. The overall structure is terminated by the ohmic contacts, emitter and collector. The device operation can be declared from the energy band in the current flow direction (z-axis) and carrier confinement directions (x- and y- axis) which contains in our case one energy state as seen in figure (23- b). When IR radiation is incident near the junction, the mobile charges (electrons) into the quantum wire active layer is moved to a higher energy state above or equal the barrier energy. These higher energy electrons can now cross into the barrier layer. Hence, photocurrent can be obtained by applying biasing voltage across the ohmic contacts to collect these generated photocarriers.

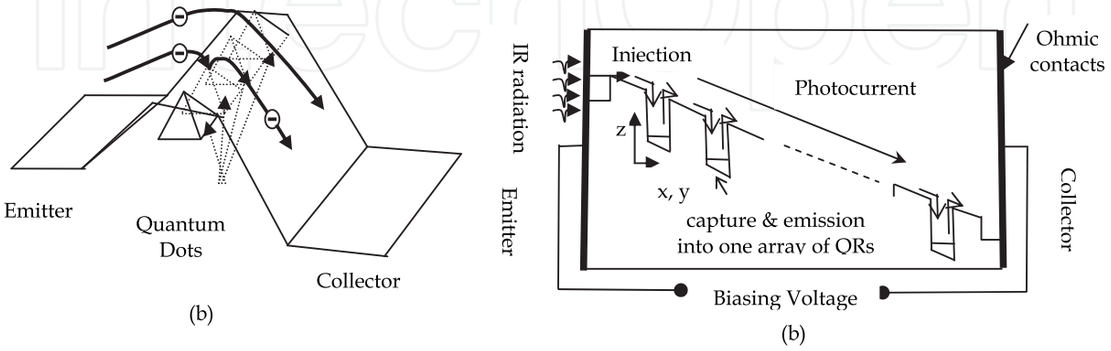

Fig. 23. (a) Conduction band profile in the QDIP and (b) QRIPs principle operation scheme (Nasr, 2007; Ryzhii & Khmyrova, 2001; Maksimović, 2003).

8. Modern advances and applications of IR photodetectors

8.1 Commercially available 320×256 LWIR focal plane arrays

Infrared imaging systems that work in 8-12 μm (LWIR) band have many applications, including night vision, navigation, flight control, early warning systems, etc. Several research groups have demonstrated the excellent performance of QWIP arrays. For example, Faska et al. (Gunpala et al., 2001) have obtained very good images using a 156×256 bound-to-miniband MQW FPA. The first 256×256 LWIR hand-held imaging camera was demonstrated by (Guapala et al., 1997). The device structure of this commercially a available FPA consisted of a bound-to-quasibound QWIP containing 50 periods of a 45 Å well of GaAs (doped n=4×10^{17} cm^{-3}) and a 500A barrier of $Al_{0.3}Ga_{0.7}As$. Ground state electrons are provided in the detector by doping the GaAs well layers with Si. This Photosensitive MQW structure is sandwiched between 0.5 μm GaAs top and bottom contact layers doped n=5×10^{17} cm^{-3}, grown on a semi-insulating GaAs substrate by MBE. Then a 0.7-μm thick GaAS cap layer on top of a 300Å $Al_{0.3}Ga_{0.7}As$ stop-etch layer was grown in stu on top of the device structure to fabricate the light coupling optical cavity.

The detectors were back illuminated through a 45° polished facet and a responsivity spectrum is shown in Fig. 24. The responsivity of detector peaks at 8.5 μm and the peak responsivity (Rp) of the detector is 300mA/W at bias V_B=*-3V*. The spectral width and the cutoff wavelength are Δλ/λ=10% and λ_c=8.9 μm, respectively. The measured absolute peak responsivity of the detector is small, up to about V_B=*-0.5V*. Beyond that it increase nearly linearly with bias reaching R_P=*380mA/W* at V_B=*-0.5V*. The peak quantum efficiency was 6.9% at bias V_B=*-1V* for a 45° double pass. The lower quantum efficiency is due to the lower well doping density (5×10^{17} cm^{-3}) as it is necessary to suppress the dark current at the highest possible operating temperature (Guapala et al., 1997).

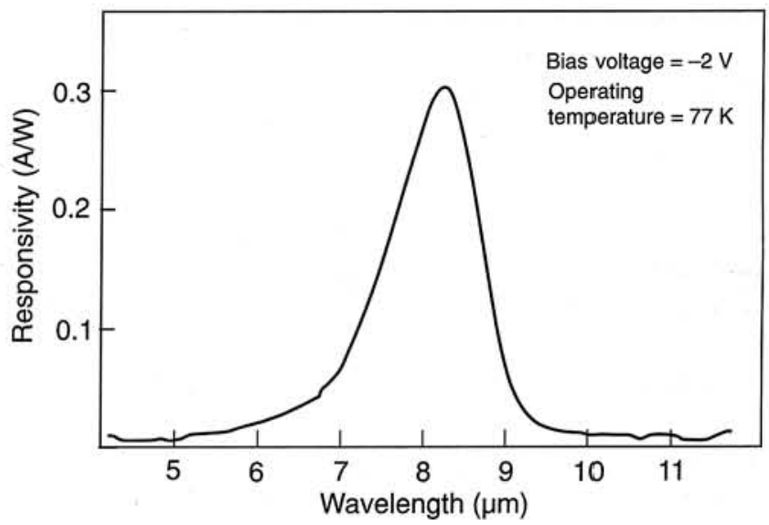

Fig. 24. Responsivity spectrum of a bound-to-quasibound LWIR QWIP test structure at temperature *T=77K*. The spectral response peak is at *8.3 μm* and the long wavelength cutoff is at *8.8 μm* (Guapala et al., 1997).

8.1.1 A 640×486 long-wavelength camera

By the same previous procedure, the camera can be established. A 640×486 QWIP FPA hybrid was mounted onto an 84-pin lead-less chip carrier and installed into a laboratory dewar which is cooled by liquid nitrogen to demonstrate a LWIR imaging camera (Guapala et al., 2001). Fig. 25 shows a frame of video image taken with this long-wavelength camera. This image demonstrates the high sensitivity of the camera. This high yield is due to the excellent GaAs growth uniformity and the mature of GaAs processing technology.

Fig. 25. This picture was taken at the night (around midnight) and it clearly shows where automobiles were parked during the daytime. This image demonstrates the high sensitivity of the 640×486 long-wavelength QWIP staring array(Guapala et al., 1998).

8.2 640×486 long-wavelength dualband imaging camera

The LWIR and very long-wavelength infrared (VLWIR) dualband QWIP device structure described in this section processed into interlace simultaneously readable dualband FPAs (i.e., odd rows for colour and the even rows for the other colour) (Guapala et al., 1999).. The device structure consists of a 30 periods stack, of VLWIR QWIP structure and a second 18 periods stack of LWIR QWIP separated by a heavily doped 0.5 μm thick intermediate GaAS contact layer. The first stack (VLWIR) consists of 30 periods of a 500Å $Al_xGa_{1-x}As$ barrier and a 60 Å GaAs well. Since the dark current of this device structure is dominated by the longer wavelength portion of the device structure, the VLWIR QWIP structure has been designed to have a bound-to-quasibound intersubband absorption peak at 14.5 μm. The second stack (LWIR) consists of 18 periods of a 500 Å $Al_xGa_{1-x}As$ barrier and a narrow 40Å GaAs well. This LWIR QWIP structure has been designed to have a bound-to-continuum intersubband absorption peak at 8.5 μm, since photo current and dark current of the LWIR device structure is relatively small compared to the VLWIR portion of the device structure, this whole dualband QWIP structure is then sandwiched between 0.5 μm GaAs top and bottom contact layers doped with $n=5\times10^{17}cm^{-3}$, and has been grown on a semi-insulating GaAs substrate by MBE. Then a 300Å $Al_{0.3}Ga_{0.7}As$ stop-etch layer and a 1.0 μm thick GaAs cap layer were grown *in situ* on top of the device structure.

GaAs wells of the LWIR and VLWIR stacks were doped with $n=6\times10^{17}$ and 2.5×10^{17} cm^{-3} respectively. All contact layers were doped to $n=5\times10^{17}$ cm^{-3}. The GaAs well doping density of the LWIR stack was intentionally increase by a factor of two to compensate for the reduced number of quantum wells in the LWIR stack (Guapala et al., 1999). It is worth noting that, the total (dark + photo) current of each stack can be independently controlled by carefully designing the position of the upper state, well doping densities, and the number of periods in each MQW stack. All of these features were utilized to obtain approximately equal total currents from each MQW stack. Two different 2D periodic grating structures were designed to independently couple the 8-9 and 14-15μm radiation into detector pixels in even and odd rows of the FPAs, the FPA fabrication process is described in detail into(Guapala et al., 1999). Video images were taken at a frame rate of 30 Hz at temperatures as high as T=74K, using a capacitor having a charge capacity of 9×10^6 electrons (the maximum number of photoelectrons and dark electrons that can be counted in the time taken to read each detector pixel). Fig. 26 shows simultaneously acquired 8-9 and 14-15 μm images using this two-colour camera (Guapala et al., 1999).

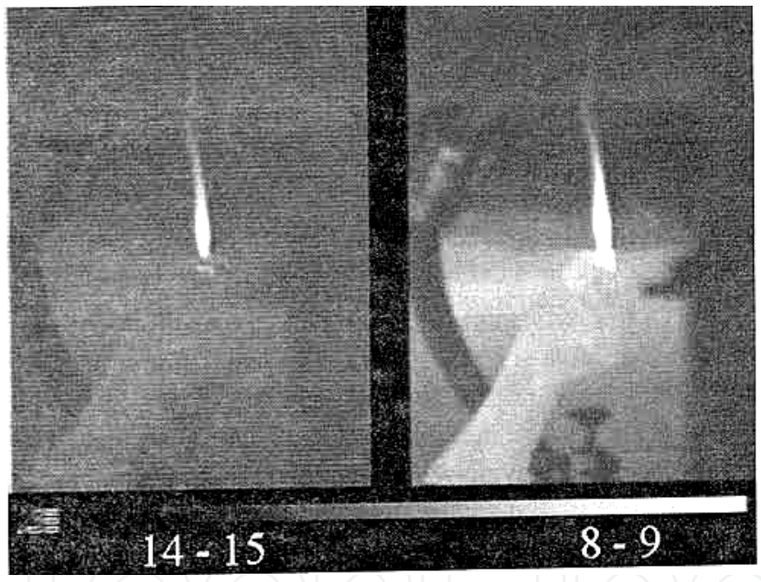

Fig. 26. Both pictures show (flame-simultaneously acquired) two-colour images with the 640×486 two-color QWIP camera. Image on the left is from 14-15μm IR and the image on the right is from 8-9 μm IR. Pixel pitch of the FPA is 25μm. The 14-15 μm image is less sharp due to the diffractions limited spot size being larger than the pixel pitch of the FPA (Guapala et al., 1999).

8.3 Broad-band QWIPs

A broad-band MQW structure can be designed by repeating a unit of several quantum wells with slightly different parameters such as quantum well width and barrier height. The first device structure (shown in Fig. 27 demonstrated by (Bandara et al., 1998a) has 33 repeated layers of GaAs three-quantum-well units separated by L_B ~575 Å thick $Al_xGa_{1-x}As$ barriers (Bandara et al., 1998b).

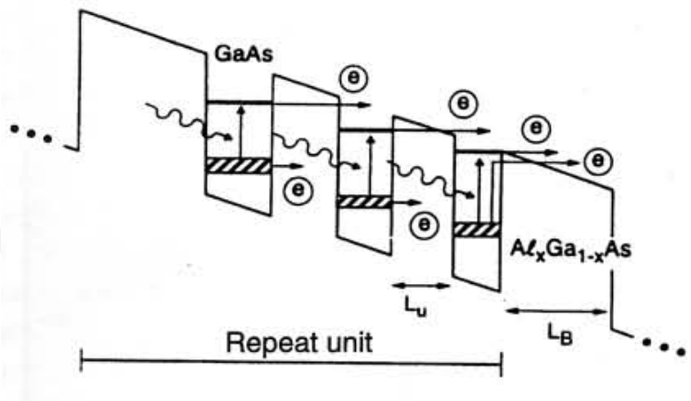

Fig. 27. Schematic diagram of the conduction band in broadband QWIP in an externally applied electric field. The device structure consists of 33 repeated layers of three-quantum-well units separated by thick $Al_xGa_{1-x}As$ barriers. Also shown are the possible paths of dark current electrons and photocurrent electrons of the device under a bias (Bandara et al., 1998a).

The well thickness of the quantum wells of three-quantum-well units are designed to respond at peak wavelengths around 13, 14, and 15μm respectively. These quantum wells are separated by 75Å thick $Al_xGa_{1-x}As$ barriers. The Al mole fraction (x) of barriers throughout the structure was chosen such that the λ=13μm quantum well operates under bound-to-quasibound conditions. The excited state energy level broadening has further enhanced due to overlap of the wave functions associated with excited states of quantum wells separated by thin barriers. Energy band calculations based on a two band model shows excited state energy levels spreading about *28 meV*. The unique characteristic of this instrument (besides being small and efficient) is that it has one instrument line shape for all spectral colours and spatial field positions. By using broad-band QWIP arrays with wavelength out to 16μm, the next version of this instrument could become the first compact, high resolution thermal infrared, hyper-spectral imager with a single spectral line shape and zero spectral smile. Such an instrument is in strong demand by scientists studying earth and planetary science.

8.4 Applications

8.4.1 Fire fighting

Video images were taken at a frame rate of 60Hz at temperature as high as *T=70K*, using a ROC (over current resistor) capacitor having a charge capacity of 9×10^6 electrons. This infrared camera helped a Los Angles TV news crew get a unique perspective on fires that raced through the Southern California seaside community of Malibu in October, 1996. The camera was used on the station's news helicopter. This portable camera features IR detectors which cover longer wavelengths than previous portable cameras could. This allows the camera to see through smoke and pinpoint lingering hotspots which are not normally visible (Guapala et al., 2001). This enabled the TV station to transmit live images of hotspots in areas which appeared innocuous to the naked eye. These hotspots were a source of concern and difficult for firefighters, because they could flare up even after the fire appeared to have subsided. Fig. 28 shows the comparison of visible and IR images of a just burned area as seen by the news crew in nighttime. It works effectively in both daylight and nighttime conditions. The event marked the QWIP camera's debut as a fire observing device.

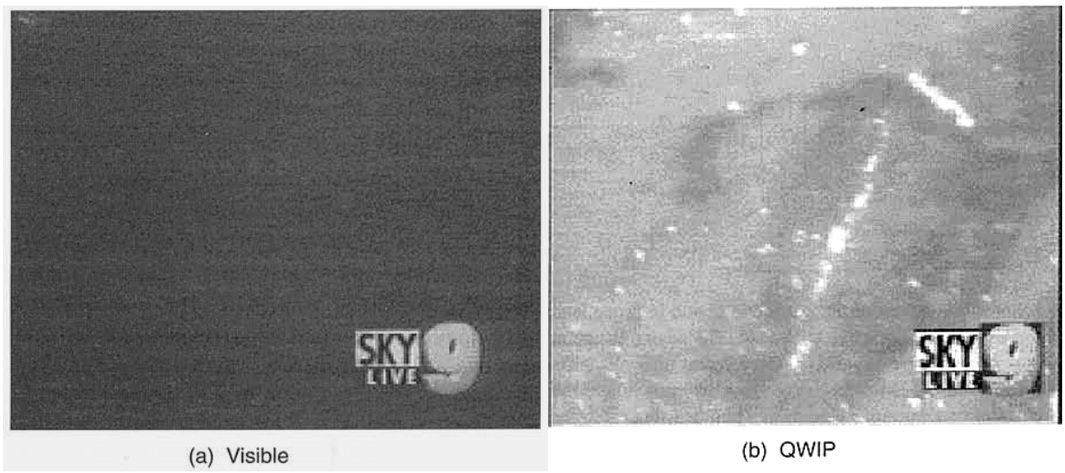

Fig. 28. Comparison of visible and IR images of a just burned area as seen by a highly sensitive visible CCD camera and the long wavelength IR camera at nighttime. (a) Visible image from a CCD camera. (b) Image from the 256×256 portable QWIP camera. This portable camera features IR detectors covers longer wavelengths than previous portable cameras could (Guapala et al., 2001).

8.4.2 Volcanology

Recently, the camera has been used to observe volcanoes, mineral formations, weather and atmospherics conditions. This QWIP camera was taken to the Kilauea Volcano in Hawaii. The objectives of this trip were to map geothermal feature. The wide dynamic range enabled us to image volcanic features at temperatures much higher (300-1000K) than can be imaged with conventional thermal imaging systems in the 3-5μm or in visible. Fig. 29 shows the comparison of visible and IR images of the Mount Kilauea Volcano in, Hawaii. The IR image of the volcano clearly shows a hot lava tube running underground which is not visible to the naked eye (Guapala et al., 2001).

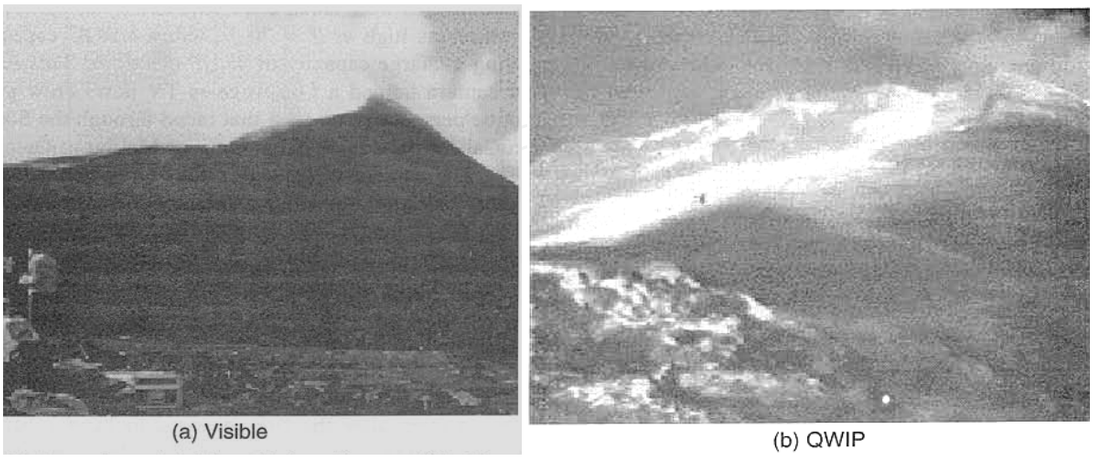

Fig. 29. Comparison of visible and IR images of the mount Kilauea Volcano in, Hawaii. (a) Visible image from a highly sensitive CCD camera. (b) Image from the 256×256 portable QWIP camera. This demonstrates the advantages of long wavelength IR in geothermal mapping (Guapala et al., 2001).

8.4.3 Medicine

Studies have determined that cancer cells exude nitric oxide. This causes changes in blood flow in tissue surrounding cancer that can be detected by a sensitive thermal sensor. Recently, OmniCorder Technologies, Inc., Stony Brook, N.Y. has developed an instrument called the BioScan System TM based on developed QWIP FPA technology. In this instrument a mid format QWIP FPA is used for Dynamic Area Telethermometry (DAT)(Bandara et al., 1998b). DAT has been used to study the physiology and patho-phy-siolgy of cutaneou perfusion, which has many clinical applications. DAT involves accumulation of hundreds of consecutive IR images and fast Fourier Transform (FFT) analysis of the biomodulation of skin temperature, and of the microhomogeneity of skin temperature (HST, which, measures the perfusion of the skin's capillaries). The FFT analysis yields the thermoregulatory frequencies and amplitudes of temperature and HST modulation.

To obtain reliable DAT data, one needs an IR camera in the larger 8μm range (to avoid artifacts of reflections of modulated emitters in the environment) a repetition rate of 30 Hz allowing accumulation of a maximal number of images during the observation period (to maximize the resolution of the FFT). According to these researches on the longer wavelength operation, higher spatial resolution, higher sensitivity and greater stability of the QWIP FPAs made it the best choice of all IR FPAs.

The two technologies work together to image the target area and to provide the physician with immediate diagnostic information. It causes no discomfort to the patient and uses no ionizing radiation. Basically, the digital sensor detects the IR energy emitted from body, thus "seeing" the minute differences associated with blood flow changes.

This camera has also been used by a group of researchers at the University of Southern California in brain surgery, skin cancer detection, and leprosy patients. In brain tumour removal a sensitive thermal imager can help surgeons to find small capillaries that grow towards the tumour due to angiogenesis (see Fig. 30). In general cancerous cells have high metabolic rate and these cancerous cells recruit new blood supply; one of the characteristic of a malignant lesion. Therefore, cancerous tissues are slightly warmer than the neighboring healthy tissues. Thus, a sensitive thermal imager can easily detect malignant skin cancers (see Fig. (31- a, and b)).

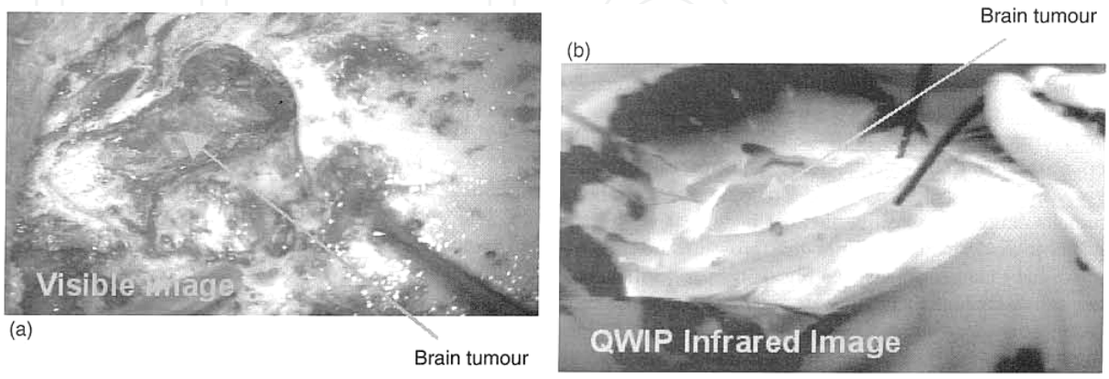

Fig. 30. (a) Visible image of a brain tumour (most of the cancerous cells are dead due to cancer sensitive drugs). (b) The thermal IR image clearly discriminate the healthy tissues from dead tissues (Bandara et al., 1998b).

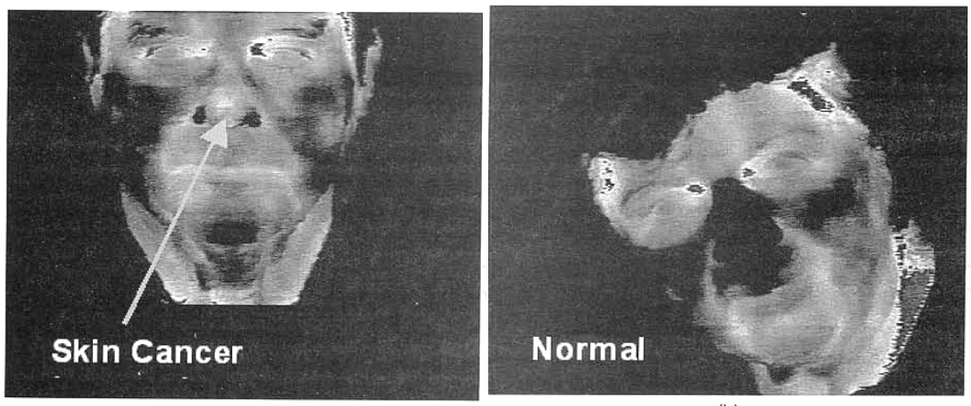

Fig. 31. (a) This clearly shows the tip of the nose is warmer than its surrounding tissues due to the enhanced metabolic activity (angiogenesis) of a skin cancer. (b) Shows a face with no skin cancer on the nose. Usually, nose and ears are colder relative to other parts of the face, because those are extending out the body (Bandara et al., 1998b).

8.4.4 Defence

It is not necessary to explain how real time IR is important in surveillance, reconnaissance and military operations. The QWIP RADIANCE was used by the researchers at the Ballistic Missile Defence Organization's innovative science and technology experimental facility in a unique experiment to discriminate and clearly identify the cold launch vehicle from its hot plume emanating from rocket engines.

Usually, the temperature of cold launch vehicles is a bout 250K, whereas the temperatures of the hot plume emanating from launch vehicle can reach 950 K. According to the plank's blackbody emission theory, the photon flux ratio of 250K and 950K blackbodies at 4μm is about 25,000, whereas the same photon difference at 8.5micm is about 115. Therefore, it is very clear that one must explore longer wavelengths for better cold-body versus hot plume discrimination, because the highest instantaneous dynamic range of IR cameras is usually 12-bits (i.e., 4096) or less. Fig. 32 shows an image of delta-II launch taken with QWIP RADIANCE camera. This clearly indicates the advantage of long-wavelength QWIP cameras in the discrimination and identification of cold launch vehicles in the presence of hot plume during early stage of lunch (Guapala et al., 2001).

Fig. 32. Image of a Delta-II launch vehicle taken with the long-wavelength QWIP RADIANCE during the launch (Guapala et al., 2001).

8.4.5 Astronomy

In this section, astronomical observation with a QWIP FPA is studied (Guapala et al., 2001). A QWIP wide-field imaging multi-colour prime focus IR camera (QWICPIC) is utilized. Observations were conducted at the five meter Hala telescope at MT. Palomar with QWICPIC based on 8-9 μm 256×256 QWIPs FPA operating at $T=35K$. The ability of QWIPs to operate under high photon background without excess noise enables the instrument to observe from the prime focused with a wide 2′×2′ field of view, making this camera unique among the suite of IR instruments available for astronomy. The excellent 1/f noise performance of QWIP FPAs allows QWICPIC to observe in a slow scan strategy often required in IR observations from space. Fig. 33 compares an image of a composite near-IR image (a) obtained by Two Micron All Sky Survey (2MASS), with an 8.5 μm long-wavelength IR image (b) obtained with a QWIPFPA at primary focus of the Palomar 200-inch hale telescope. The S106 region displays vigorous star-formation obscured behind dense molecular gas and dust heated by star light. Thermal-IR imaging can be used to assess the prevalence of warm (~300K) dusty disks surrounding stars in such region. Formations of these disks are an evolutionary step in the development of planetary systems. These images demonstrate the advantage of large format, stable (low 1/f noise) LWIR QWIP FPAs for surveying obscured regions in search for embedded or reddened objects such as young forming stars.

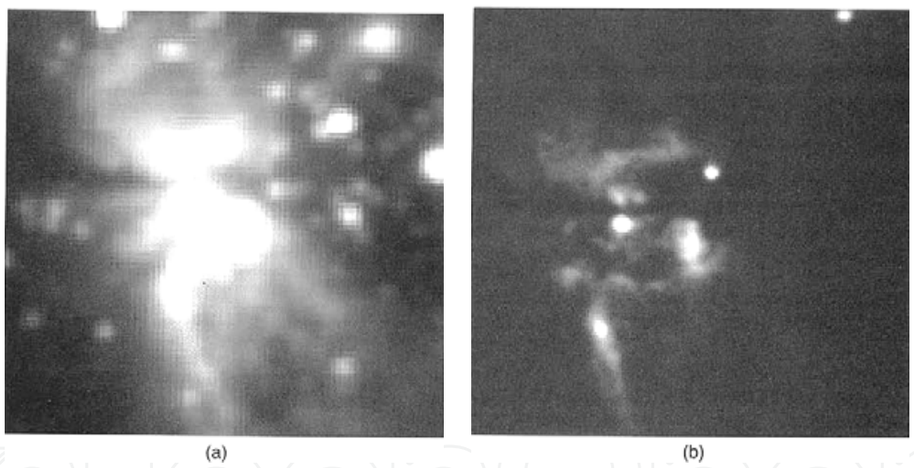

Fig. 33. Compares an image of a composite near-IR image (a) obtained by 2MASS, with an 8.5 μm long-wavelength IR image (b) obtained with a QWIPFPA at primary focus of the Palomar 200-inch hale telescope (Guapala et al., 2001).

9. Summery and conclusions

After previous discussions, one can interpret the importance of the photodetectors as a first part of any system-detection. This system-detection can be altered according to the covered range of photodetectors. By another meaning these applications are varied corresponding to their spectrum wavelengths. There are mainly two types, one of them is the infrared photodetectors which covered middle, long, ultra or far long wavelengths, (750- ~10^5nm). Another one is ultra violet photodetectors which covered shortest and short wavelengths, (~100 to 365 nm).

The study is concentrated to the semiconductor-based photodetectors. In the case of IR photodetectors, its interest is based on different fields of its applications such as night vision, medicine, space communications, missiles, and so on. The neediest of qualified IR detectors directed the researchers toward developing new constructions that denote a facility of mass production. The main advantage of the traditional commercial photodetectors is that they can be operated at room temperature. However the main problem is the complexity of fabrication. Moreover, the soften materials which it can be utilized. Other drawbacks can be recognized from traditionally p-i-n structure series is how one can balance between the response time; depending on the width of layer, and the required gain or amplification. So, the thinking is intended for overcome the previous problems. The ideas are how to obtain the crystal layers which offer a small energy gap between the valance and conduction bands. Also, how one can obtain both of fast detectors response time and gain. Moreover, the problem of fabrications blocked the growth in this direction of the bulk IR detectors. The solution is to transfer from inter-band translation (bulk) to intersubband translation (quantum). That means that electron or holes should be quantized. The number of freedom of mobile charge determines the type of IR photodetector. There are three types of quantum IR photodetectors (QIRPDs). The quantum dot IR photodetectors (QDIPs), the degree of freedom is zero. The quantum wire IR photodetectors (QRIPDs), the degree of freedom is one. The last type is quantum well IR photodetectors (QWIPs) the degree of freedom is two. Although the quantum detectors indicate an easier way of fabrication and mass production, it suffers from many drawbacks which depend on the nature of freedom into quantum detectors. For example, QWIPs suffer from coupling and lower gain. The coupling problem and gain are processed by much research groups and they are trying to overcome by utilizing corrugated quantum well and focal plane arrays (FPAs) as discussed before. In QDIPs, the problem of coupling is eliminated as it is response to the normal radiations. Meanwhile it suffers from high dark current. The last one is QRIDs, it denotes smaller dark current comparing with quantum dot detectors. It opens the way to enhance the performance of IR detectors. The performance parameters can be summarized to responsivity, quantum absorption efficiency, and detectivity. The theoretical details of the dependence of these photodetectors performance parameters into quantum detectors parameters are studied before in previous articles (Aboshosha et al., 2009; Aboshosha et al., 2009b; Abou El-Fadl et al., 1998; Eladle et al., 2009; Nasr, El_mashade, 2006; El_mashade et al., 2003; El_mashade et al., 2005; Future Technologies Division, 2003; Nasr, 2011; Nasr, 2011b; Nasr, 2009; Nasr et al., 2009; Nasr, 2008; Nasr,2006; Nasr & Ashry; 2000; Nasr, 2007). From the obtained results, the QWIPs give high responsivity which mean smaller values of dark current in corresponding to other types.

Another type of semiconductor-based detectors is UV ranged photodetectors. It is evident to consider the fact that, here, the energy gap is not small in contrast to IR detectors. So, the modern advances in UV photodetectors will be based on enhancing the p-n detector performance. Such as, the wide range which can be covered or higher temperature which can be operated or recent mixture composition which can be obtained.

On the other hand, One-dimensional UV semiconductor nanowires and nanorods have also attracted great attention because of their potential applications in both nanoscale electronic and optoelectronic devices. Compared with bulk or thin film photodetectors, 1-D photodetectors should be able to provide a large response due to their larger aspect ratio of length to diameter and high surface to volume ratio.

The importance of UV photodetector is related to its application as described before for solar UV detection, visible blind detection, missile warning, space communication and flame sensing.

The modern advanced IR phodetectros are built on utilizing QWIPDs FPAs which denote many features. For example, they give higher resolution and performance. Also, they become commercially available now.

The development in the case of QWIPs FPAs will be done by multi techniques. Such as, by solving quantum well by dot or/ and wire layer FPAs. Another technique can be recognized is to utilize a hybrid composition from well and dot layer which is known as quantum-dot-in–a-well (DWELL FPAs) detectors as given in the next section. This DWELL FPAs can combine the advantage of both of well and dot quantum types. That it can achieve a response to the normal incident IR rays in the case of QD and high responsivity in the case of QW.

10. Future prospects

Firstly, all applications considered before can utilize quantum dot and quantum wire infrared photodetectors in place of quantum well. That can be done by replacing each one well by one array of QDs or QRs. Practical applications of QDIPs are beginning to widespread in different fields. Later one, QRIPs is still under investigation phase but from my research background, it will give improved performance in comparison with QDIPs. Because of it denotes less than dark current and can cover wide range from IR spectrum (Nasr, 2007, Nasr, 2011). Moreover as discussed in (Nasr, 2009), the future of IR detectors is directed to exploit the advantages of FPAs in the reminder of IR quantum devices such as QDIPs and QRIPs. Additionally, recent articles are exposed to fabricate Long-Wave Infrared Quantum-Dots-in-a-Well detector as in (Pucicki et al., 2007; Andrews et al., 2009) and held comparison with FPAs as shown in Fig. 34. The results encourage developing a devices by the same way to combine the advantages of each quantum devices. Design and fabricate a broadband 8-14 μm infrared *1K×1K*, GaAs Quantum Well Infrared Photodetector (QWIP) imaging array is important point for enhance the performance as in (Buckner, 2008).

On the other hand, related to photodetectors that acquired our interest, there are quantum laser sources and modulators that move in the same direction and still need more studies now and in the next projects of nanotechnology devices.

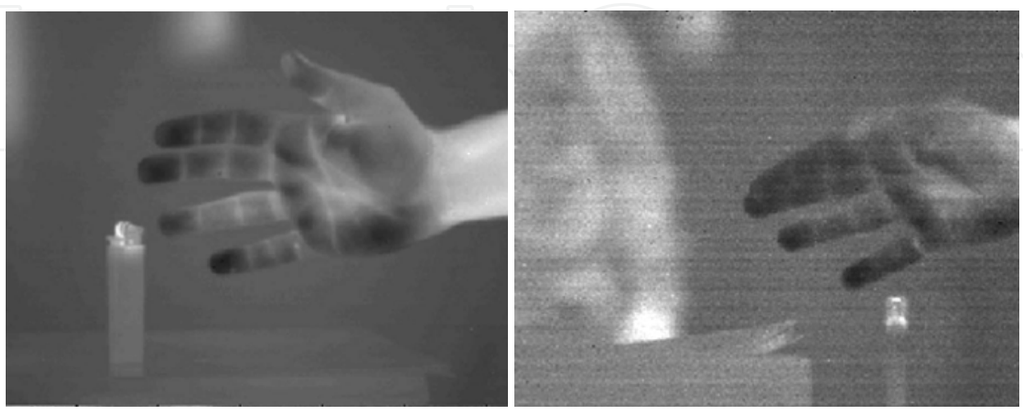

Fig. 34. Nonuniformity-corrected images obtained with the (left) QWIP and (right) DWELL FPA cameras at 60 K of a cigarette lighter on or near a book. The right image also has a person walking in the background (Andrews et al., 2009).

11. References

Aboshosha et al. (2009a). Precise Autonomous Rescuing relying on Integrated Visual and IR Detection Technique. *J. of Engineering & Computer Sciences; QUJECS*, Vol. 2, No.3

Aboshosha et al. (2009b). Improved Thermographic Object Detection Relying-on Image Processing and Sensorial Development of Quantum IR Photodetectors. *Menofia J. of Electronic Engineering Research (MJEER)*, Vol. 19, No.1&2, pp. 63-80

Abou El-Fadl et al. (1998). Computer Aided Analysis of Multimode Planar Graded-Index Optical Waveguides. the 2nd IMACS , International Multiconference CESA'98 Nabeul-Hammamet, Tunisia. April 1-4

Anbar et al. (1999). Babalola, "Clinical Applications of DAT Using a QWIP FPA Camera. *Proc. SPIE 3698*, p. 93-102

Andrews et al. (2009). Comparison of Long-Wave Infrared Quantum-Dots-in-a-Well and Quantum-Well Focal Plane Arrays. *IEEE Trans. on Electron Devices*, Vol.56, No. 3, 2009.

Bandara et al. (1998a). 10-16 μm Broad-Band Quantum Well Infrared Photodetectors. *Appl. Phys. Lett.*, Vol.72, pp. 2427-2429

Bandara et al. (1998b). 10-16 μm Broad-Band Quantum Well Infrared Photodetectors," Proc. SPIE, 3379, 396-401

Brune, H. (2001). Encyclopedia of Materials: Science and Technology. *Elsevier S*, pp. 3683-3693

Buckner, J. L. (2008). HyspIRI Technology Investment Overview. *Earth Science Technology Office*, NASA

Campbell et al. (1983). High-Performance Avalanche Photodiode with Separate Absorption,. 'Grading' and Multiplication Regions. *Electron Lett.* Vol.19, pp. 818-820

Capasso, F. (1985). Physics of Avalanche Photodiodes. *in Semiconductor and Semimetals*, part D, W. T. Tsang, Ed., Academic Press, Orlando, FL, Vol. 22, pp. 1-172

Chang, C. Y. & Francis Kai, (1994). GaAs High Speed Devices. *John Wiley & Sons*

Coleman, J. J. (1997). Metalorganic Chemical Vapor Deposition for Optoelectronic Devices" proceedings of IEEE, Vol.85

Das, B. & Singaraju, P. (2005). Novel Quantum Wire Infrared Photodetectors. *Infrared Physics & Technology*, Vol. 46, pp. 209-218

Donkor, E. (2004). GaAs-Based Nanodevices. *Encyclopedia of Nanoscience and Nanotechnology*, Vol. 3, pp. 703-717

El_Mashade et al. (2003). Characteristics Determination of Quantum Well Infrared Photodetectors. *IEEE Mediterranean Microwave Symposium*, pp. 29-40

El_Mashade et al. (2003).Theoretical Analysis of Quantum Dot Infrared Photodetectors. *J. Semicond. Sci. Technol.* Vol. 18, p. 891-900, UK

El_Mashade et al. (2005). Performance Analysis of Quantum Well Infrared Photodetectors. *J. of Optical Communications*, Vol. 3, pp. 98-110, Germany, Mar. 2005.

Eladl et al. (2009). Dynamic Characteristics of QWIP-HBT-LED Optoelectronic Integrated Devices" J. of Semiconductor Phys., Quantum Electronics & Optoelectronics, Vol. 12, No. 3. pp. 260-263

Fox, M., (2001). Optical Properties of Solids. *Oxford University*

Future Technologies Division, 2003. Applications of Nanotechnology in Space Developments and Systems. Published by *VDI Technology Center*, No. 47, Düsseldorf, Germany

Guapala et al. (1997). 9 μm Cutoff 256×265 *GaAs/ $Al_xGa_{1-x}As$* Quantum Well Infrared Photodetectors Hand-Held Camera. *IEEE trans. Electron devices*, Vol. 44, pp. 51-57

Guapala et al. (1998). Long-Wavelength 640×486 *GaAs/ $Al_xGa_{1-x}As$* Quantum Well Infrared Photodetectors Snap Shot Camera. *IEEE Trans. Electron Dev.*, Vol. 45, pp. 1890-1895

Guapala et al. (1999). 8-9 and 14-15 μm Two Color 640×486 *GaAs/ $Al_xGa_{1-x}As$* Quantum Well Infrared Photodetectors (QWIP) Focal Plane Array Camera. *Proc. SPIE*, 3698, pp. 687-697

Gunpala et al. (2001). Recent Development and Applications of Quantum Well Infrared Photodetectors Focal Plane Arrays. *J. Optoelect. Review*, Vol.9, No.2, pp.150-163

Hsueh et al. (2007). Crabwise ZnO Nanowire UV Photodetector Prepared on ZnO" : Ga/Glass Template. *IEEE Trans. on Nanotech.*, Vol. 6, No. 6, pp. 595-600

Johnson et al. (1984. A MOCVD Reactor Safety System for a Production Environment. *Journal Crystal Growth*, Vol. 68, pp. 497-501

Jung et al. (2006) . Circuit Fabrication at 17 nm Half-Pitch by Nanoimprint Lithography. *Nano Lett.* Vol. 6, No. 351

Kasper, B. L. & Campbell, J. C. (1987). Multigigabit-per-Second Avalanche Photodiode Lightwave Receivers. *J. Lightw. Technol.* LT-5, pp. 1351-1364

Krost et al. (1999). X-Ray analysis of Self-Organized InAs/InGaAs Quantum Dot Structure. *Cryst. Res. Technology*, Vol. 34, pp. 89-102

Lee et al. (2005. Epitaxial Growth of a Nanoscale, Vertical-facet, High Aspect Ratio, One-Dimensional Grating in III-V Materials for Integrated Photonics. *Appl. Phys. Lett.*, Vol. 87, 071110-1-3

Levine, B. F. (1993). Quantum Well Infrared Photodetectors. *J. Appl. Phys.*, Vol. 74, pp. 7-121

Liang et al. (2006). InGaAs Quantum Dots Grown on B-type High Index GaAs Substrates: Surface Morphologies and Optical Properties", Nanotechnology, 17, pp. 2736-2740.

Liu et al. (1993). Fabrication of Quantum Dots Using Insitu Etching and Regrowth During MBE Growth. *IEEE,* 1993.

Liu, H. C. (1992). Noise Gain and Operating Temperature of Quantum Well Infrared Photodetectors. *Appl. Phys. Lett.*, Vol. 61, pp. 2703-2705

Maksimović, M. (2003). Quantum Dot Infrared Photodetector as an Element for Free-Space Optical Communication Systems. Xi Telekomunikacioni Forum TEL For, Beograd, Sava centar, Vol.11, pp.25-27

Manasevit, H. M. (1968). Single-Crystal Gallium Arsenide on Insulating Substrates. *A Physics Letter*, Vol. 12, No 4, pp. 156-159

Melchior, H. (1977). Demodulation and. Photodetection Techniques. *Laser Handbook*, Vol.1, F. T. Arecchi and E. O. Schulz-Dubois, Eds., North-Holland, Amsterdam, 1972, pp. 725-835; Phys. Today, Vol. 30, No.12, 32

Muhammad et al. (2007). Epitaxial Method of Quantum Devices Growth. *Ibnu Sina Institute for Fundamental Science Studies*, Malaysia

Nai-Chang, Y. (2008). A Perspective of Frontiers in Modern Condensed Matter Physics" AAPPS Bulletin, Vol. 18, No. 2, pp. 1-19

NASA (1999). Report of UV/O Working Group

Nasr et al. (2006). "Dark Current Characteristics of Quantum Wire Infrared Photodetectors," IEE Proc. Optoelectronic J., Vol.1, No. 3, pp. 140–145

Nasr et al. (2009). Theoretical Characteristics of Quantum cascaded lasers. *J. of Engineering & Computer Sciences; QUJECS*, Vol. 2, No.2

Nasr, A. & Ashry, M. (2000). Computer Aided Analysis of TM- Multimode Planar Graded-Index Optical Waveguides and the Field Distribution. *Seventh Conference of Nuclear & Applications*, Cairo, Egypt 6-10

Nasr, A. & El_Mashade, M. (2006). Theoretical Comparison between Quantum-Well and Dot Infrared Photodetectors. *IEE Proc. Optoelectronic*, Vol. 153, No. 4, pp. 183-190

Nasr, A. (2007). Performance of Quantum Wire Infrared Photodetectors under Illumination Conditions. *Optics & Laser Technology, Elsevier*, Vol. 41, pp. 871–876

Nasr, A. (2008). Spectral Responsivity of the Quantum Wire Infrared Photodetectors. *Optics & Laser Technology, Elsevier,* Vol. 41, pp. 345– 350

Nasr, A. (2009). Theoretical Characteristics of Quantum Wire Infrared Photodetectors under Illumination Conditions. *J. of Optical Communications*, Vol. 30, Issue 3, pp. 126-132

Nasr, A. (2011). Detectivity Performance of Quantum Wire Infrared Photodetectors. *J. Opt. Commun.*, Vol. 32 No. 2 , pp. 101–106.

Nasr, A. (2011). Theoretical study of the photocurrent performance into quantum dot solar cells. *under publication*, 2011

National Nanotechnology Initiative Workshop. (2004). Nanotechnology in Space Exploration. *Report*

Norbert, K. & Jurgen, B. (2005). Guidelines for Future UV Observatories. *Institut für Astronomie und Astrophysik*, Abteilung Astronomie (IAAT), Universität Tübingen, pp. 1-6

Pauzauskie, P. J. & Yang, P. (2006). Nanowire Photonics: Review Feature. *Materials Today*, Vol. 9, No.10

Pernot et al. (1999). Improvement of Low-Intensity Ultraviolet Photodetectors. *Phys. Stat. Sol.(A)* Vol.176, pp. 147-151

Phillips et al. (1999). Self-Assembled InAs-GaAs Quantum-Dot Intersubband Detectors. *IEEE J. Quantum Electron*, Vol. 35, No. 6, pp. 936-943

Piotrowski, J. & Rogalski, A.(2007). High-Operating-Temperature Infrared Photodetectors. *SPIE Press Book*

Piotrowski, J. (2004). Uncooled Operation of IR photodetectors. *J. Optoelectronic Review*, Vol. 12, No. 1, pp. 111-122

Pucicki et al. (2007). Technology and Characterization of p-i-n Photodetectors with DQW (In,Ga)(As,N)/GaAs Active Region. *Optica Applicata*, Vol. XXXVII, No. 4

Ryzhii et al. (2000). Dark Current in Quantum Dot Infrared Photodetectors. *Jpn. J. Appl. Phys.* Vol. 39, pp. L 1283-L 1285

Ryzhii, V. & Khmyrova,I. (2001). On the Detectivty of Quantum-Dot Infrared Photodetectors. *Appl. Phys. Let.* Vol. 78, No. 22, pp. 3523-3525

Ryzhii, V. (2003). Intersubband Infrared Photodetectors. *World Scientific*, Vol. 27

Shen et al. (2000). Progress on Optimization of P-type GaAs/AlAs Quantum Well Infrared Photodetectors. *J. Vaac. Sci. Technol.* A, Vol. 18, pp. 601-604

Stillman, G. E. & Wolfe C. M.(1977). Avalanche Photodiodes. *Infrared Detectors II, R. K. Willardson and A. C. Beer, Eds.*, Vol. 12 of Semiconductors and Semimetals, pp. 291-393. Academic Press, New York

Sze, S. M. (1981). Physics of Semiconductor Devices. *Wiley*, New York

Tarif, L. E. (1991). Planar InP/InGaAs Avalanche Photodiodes with a Gain-Bandwidth Product Exceeding 100 GHz. *Proc. Optical Fiber Common. Conf.*, Optical Society of America, Washington, Dc, paper ThO3, Vol. 4

Tucker et al., (1986). Coaxially Mounted 67 GHz Bandwidth InGaAs PIN Photodiode. *Electron. Lett.*, Vol. 22, No. 17, pp. 917-918

URL http://www.its.caltech.edu/~feynman/

Waleker et al. (2007). The development of nitride base UV photodetectors. *J. Optoelectronic Review*, Vol. 8, No. 1, 2000.

www.nanoforum.org (2007). Nanotechnology and Civil Security Report

Zhao, X. (2006). Carrier Transport in High-Speed Photodetectors Based on Two-Dimensional-Gas. *Thesis*

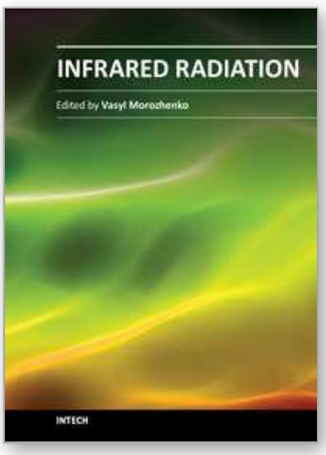

Infrared Radiation

Edited by Dr. Vasyl Morozhenko

ISBN 978-953-51-0060-7
Hard cover, 214 pages
Publisher InTech
Published online 10, February, 2012
Published in print edition February, 2012

This book represents a collection of scientific articles covering the field of infrared radiation. It offers extensive information about current scientific research and engineering developments in this area. Each chapter has been thoroughly revised and each represents significant contribution to the scientific community interested in this matter. Developers of infrared technique, technicians using infrared equipment and scientist that have interest in infrared radiation and its interaction with medium will comprise the main readership as they search for current studies on the use of infrared radiation. Moreover this book can be useful to students and postgraduates with appropriate specialty and also for multifunctional workers.

How to reference

In order to correctly reference this scholarly work, feel free to copy and paste the following:

Ashraf S. A. Nasr (2012). Infrared Radiation Photodetectors, Infrared Radiation, Dr. Vasyl Morozhenko (Ed.), ISBN: 978-953-51-0060-7, InTech, Available from: http://www.intechopen.com/books/infrared-radiation/infrared-radiation-photodetectors

INTECH
open science | open minds

InTech Europe
University Campus STeP Ri
Slavka Krautzeka 83/A
51000 Rijeka, Croatia
Phone: +385 (51) 770 447
Fax: +385 (51) 686 166
www.intechopen.com

InTech China
Unit 405, Office Block, Hotel Equatorial Shanghai
No.65, Yan An Road (West), Shanghai, 200040, China
中国上海市延安西路65号上海国际贵都大饭店办公楼405单元
Phone: +86-21-62489820
Fax: +86-21-62489821

IntechOpen